DISSERTATION

MATHEMATICAL METHODS FOR FLUID-SOLID INTERFACES:

MEANDERING STREAMS AND SAND RIPPLES

Submitted by

Keith Mertens

Department of Mathematics

In partial fulfillment of the requirements

For the Degree of Doctor of Philosophy

Colorado State University

Fort Collins, Colorado

Spring, 2008

UMI Number: 3321298

INFORMATION TO USERS

The quality of this reproduction is dependent upon the quality of the copy submitted. Broken or indistinct print, colored or poor quality illustrations and photographs, print bleed-through, substandard margins, and improper alignment can adversely affect reproduction.

In the unlikely event that the author did not send a complete manuscript and there are missing pages, these will be noted. Also, if unauthorized copyright material had to be removed, a note will indicate the deletion.
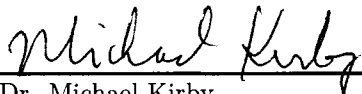
UMI®

COLORADO STATE UNIVERSITY

April 10, 2008

WE HEREBY RECOMMEND THAT THE DISSERTATION PREPARED UN-
DER OUR SUPERVISION BY KEITH MERTENS ENTITLED "MATHEMATICAL
METHODS FOR FLUID-SOLID INTERFACES: MEANDERING STREAMS AND SAND
RIPPLES" BE ACCEPTED AS FULFILLING IN PART REQUIREMENTS FOR THE
DEGREE OF DOCTOR OF PHILOSOPHY.

Committee on Graduate Work
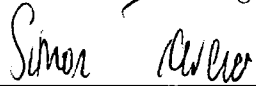
Dr. Kelly Chappell

Dr. Michael Kirby

Dr. Steve Thompson

Dr. Simon Tavener

Adviser: Dr. Vakhtang Putkaradze

Department Head: Dr. Simon Tavener

ABSTRACT OF DISSERTATION

MATHEMATICAL METHODS FOR FLUID-SOLID INTERFACES:
MEANDERING STREAMS AND SAND RIPPLES

This thesis presents several mathematical methods for modeling free surfaces, interfaces, and fluid-solid interactions. This work is done in the context of two physical systems.

In the first two sections, the focus will be to understand the the physics of streams flowing down inclined substrates. Models will be derived to investigate both steady state and dynamic meandering profiles. It will be shown that, through the right approximation techniques, many physical insights can be drawn about this system. These results include: a complete understanding of the steady states, transitions between steady states, mechanism of meandering, forces involved in meandering, and spectral scaling laws of long-time ensemble averaged meandering stream profiles.

In the third section, the focus will shift to how one can model underlying physics when it becomes too complicated to address from first principles. Here, the power of symmetries and conservation laws are explored to derive an amplitude equation describing the interface between sand and water when the water is subjected to oscillatory flow. The thesis will then close by posing a novel way to study scaling laws with respect to parameters using Lie's prolongation algorithm.

Through this work various tools will be combined from the fields of physics, engineering, applied and pure mathematics to develop approaches for reducing complex systems into tractable pieces which can be studied carefully.

Keith Mertens
Department of Mathematics
Colorado State University
Fort Collins, Colorado 80523
Spring 2008

iii

Acknowledgments

I would like to thank several people who have been essential throughout my Graduate studies. First, and foremost, Vakhtang Putkaradze, my adviser and friend. Without him none of this could have been possible. I would also like to thank my family. Without their continued support and understanding I'm not sure where I would be. I would like to thank my Committee (Kelly Chappell, Michael Kirby, Simon Tavener and Steve Thompson), it was because of their invaluable help throughout and corrections that this Dissertation is complete. I would like to thank my collaborator/mentors (Peter Vorobieff, Bjorn Birnir, and Tomas Bohr), together we have had much fun working together, and they have taught me a lot. I would like to make a special note of thanks to Teis Schnipper and Frederik Bundgaard who also worked on sand ripples project. It was because of their generous contribution of pictures from their thesis' that allows the third section looks as nice as it does. I would like to thank Steve Benoit and Amanda Urqhart for giving the draft its first read and making many suggestions and corrections. Lastly, I would like to thank God for the strength to get through this process.

Dedication

Figure 0.1: Mona Mia Mertens

This work is in the loving memory of Mona Mia Mertens, my best friend and loyal companion who stood by me through my entire academic experience. I will miss her more than words can say.

Contents

Contents

Contents

Contents

List of Figures

List of Figures

List of Figures

List of Tables

Chapter 1

Introduction

1.1 Outline

Over the course of my graduate studies, I have worked on several problems which can all loosely be classified under the field of mathematical modeling of complexity, especially relating to evolution of free-surfaces and interfaces. In general, these types of problems are highly non-linear and can exhibit a great deal of sensitivity to parameters. Therefore, writing models can be challenging. In systems exhibiting a great deal of complexity, having real experimental data to rely on becomes imperative. Hence, the types of systems I have studied are always coupled directly to experiments.

The two experiments chosen for the focus of this thesis each have a rich history with over one-hundred years of study. Nonetheless, the complexity in these systems has allowed them to be a continued source of scientific contemplation. This work serves to add a few more pieces into the puzzles of understanding these phenomena, and creating mathematical tools by which to model such complexity.

This introduction serves to outline the remaining text, giving a basic overview of the structure of this thesis. Section 1 is compromised solely of Chapter 1. It is meant to be an overview on the subject of gravity driven fluid flows down inclined surfaces.

Chapter 1. Introduction ,

There is extensive literature on this subject, so it by no means meant to be an all inclusive account. However, it is meant to set the stage for the reader about what has been done related to this work, and what was known previous to this study,

The second section is Chapters 2-6. Here, details of the current work concerning flows on inclined planes is developed. While, as stated above, there is extensive literature on this subject, there is also a large amount of controversy and conflicting statements. Papers are focused on specific experimental conditions, which are not always stated clearly, and can (have) made generalizations difficult, and at times dangerous. Therefore, this section will attempt to investigate the complexity of this problem in the broadest possible context, developing models and physical understanding for how and why this system behaves as it does.

Some of the major results found include:

- The existence of steady states is proven experimentally.

- A model of steady states is derived from first principles.

- The stationary states are subjected to perturbations and the mechanism of meandering exposed.

- The stationary state model is generalized.

- Numerical and experimental work confirm the existence of a universal power-law scaling for the long-time ensemble averages spectrum of stream profiles.

- Analogous statistics are found to real river systems, including a "Hack's law" scaling, and an analytic way to recover the observed 1.1 scaling exponent associated with the second structure function for river curvature.

The third section contains Chapters 7-8. Here, another model is developed to try to explain the dynamics of underwater sand ripples which develop when a flat bed of sand is exposed to oscillatory flow above. Due to the complexity of the problem, an amplitude equation based on conservation laws and symmetries is derived. Then the

Chapter 1. Introduction

use of Lie's prolongation algorithm is considered to investigate wavelength selection in this system.

Some of the major results of study include:

- The development of a 1D model which describes much of the required dynamics.

- Analysis of the 1D model analytically and numerically.

- A novel approach to studying non-linear wavelength selection.

Lastly, section 4 is a series of appendices meant to: clarify notation, fill in details (which are necessary) but break the flow of reading, and help future students to understand some of the details underlying important calculations.

In a more detailed and bullet form, the dissertation can be outlines as follows:

- Section 1 Introduction to inclined plane flows.

  - Chapter 1: Brief history of problem and previous work.
    Including summary of Mertens *et. al.* Nature (2004) [7] and Mertens *et. al.* J. Fluid Mech. (2005) [8].

- Section 2 An account of our research on the inclined plane problem. Includes the relevant details of Birnir *et. al.* PRL (2008 under review) [9] and Birnir *et. al.* J. Fluid Mech. (2008 under review) [10].

  - Chapter 2: Explanation of experiments performed and results

  - Chapter 3: Theoretical models are developed

  - Chapter 4: Numerical Results are presented

  - Chapter 5: Generalizations to rivers

  - Chapter 6: Future Work

- Section 3 Underwater sand ripples and Lie prolongation.
  Including details of Schnipper *et. al.* PRL (2008 under review) [11].

Chapter 1. Introduction

- Chapter 7: Brief history of problem, model developed, numerics explored, coarsening discussed

- Chapter 8: Lie Prolongation applied to 1D amplitude equation.

- Section 4 Appendices of additional supporting information including:

  - Additional Braids Derivation

  - Variational Derivative

  - Instabilities

  - Stochastic PDEs

  - Prolongation Calculation

  - Some additional notes and pictures about sand ripple experiments

  - References

SECTION I.

History, like a vast river, propels logs, vegetation, rafts, and debris; it is full of live and dead things, some destined for resurrection; it mingles many waters and holds in solution invisible substances stolen from distant soils.

Jacques Barzun

History does not unfold: it piles up.

Robert M. Adams

1.2 History

"Observe the motion of the surface of the water, which resembles that of hair, which has two motions, of which one is caused by the weight of the hair, the other by the direction of the curls; thus water has eddying motions, one part which is due to principle current, the other to the random and reverse motion."
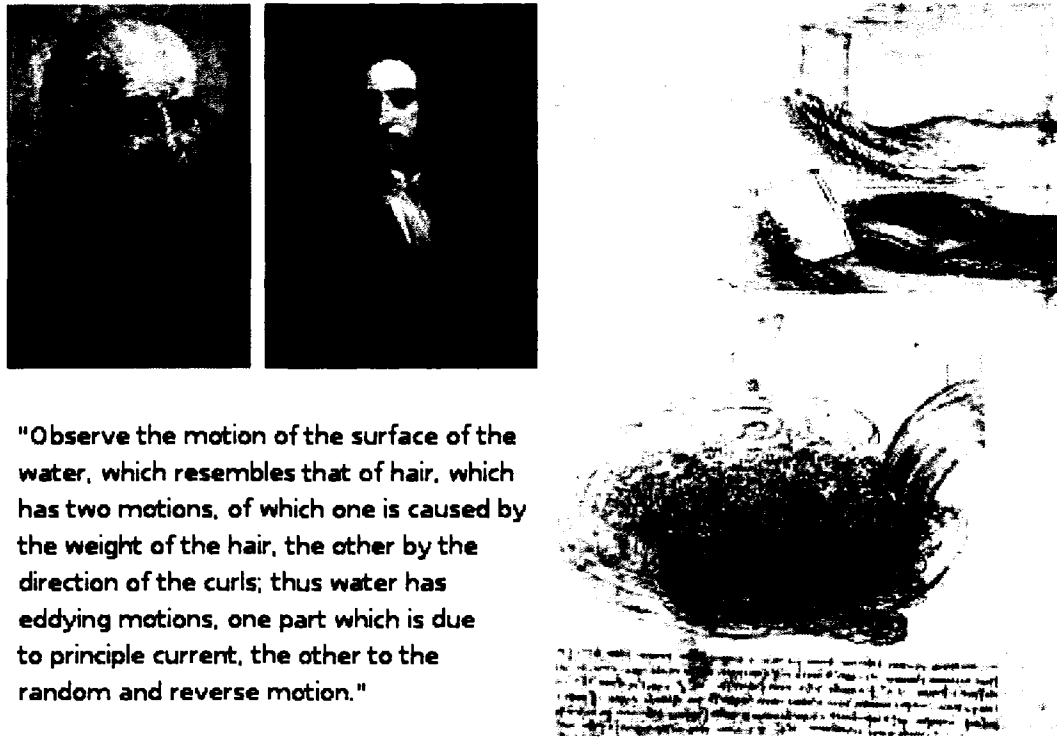
Figure 1.1: Da Vinci, Newton, and turbulence (left to right)

Fluid dynamics has been an important area of study since Newton in the early 1700's. Even Da Vinci was compelled to contemplate turbulence in fluids before the vocabulary was invented. After the invention of calculus, some of the strongest minds in science (such as Euler, Cauchy, Laplace, Lagrange, Poincare, Navier, Stokes, Kolmogorov, and Einstein) dedicated time from their lives to consider this specific subject. Why? In addition to the fact that the world around us is replete with hydrodynamic processes, additionally it is the most common natural phenomenon which will not lend itself easily to linear theory. This is, of course, followed closely by the fact that fluid dynamics is one of the most natural situations in which to visualize non-linear systems and the rise to their complexity. While the area of fluid dynamics has this long history, with combined contributions from numerous great minds, it is still an area of active research and some of the most basic questions, such as whether or not a solution even exists to the general three-dimensional Navier-Stokes

equations, still remain unanswered.

Another fundamental question in fluid dynamics is that of flow stability and pattern formation under the influence of various types of boundaries when driven by gravity. The interest in this problem comes from the fact that this is a common setting in both nature and industry. Even a seemingly "simple" question gives rise to such complexity that, while much effort has been conducted towards a complete model, a full understanding of the phenomenon has thus far eluded the scientific community.

Even answering the simple question of whether or not a flow could achieve a straight stationary state while flowing down an incline remained unanswered until recently, see for example Perazzo *et. al.* [12], Mertens *et. al.* [7], [8]. Many people believed it was an inherent instability of the flow itself, see for example Parker [13], Mizumura [14]. Much of the difficulty in this problem arises from the fact that a true understanding of these flows requires a complete model of turbulence, as well as of the delicate interactions between fluids and substrate boundaries. Even if the boundary is non-mobile (non-erosive), microscopic interaction can still give rise to complications including contact angle hysteresis. The true nature of the contact angle is quite complicated, for a fundamental reference see DeGennes [15]. Because theories on these subjects are still incomplete, a detailed model remains impossible.

It will be shown through this thesis, however, that with the use of data collected with a highly controlled experiment, and the use of several valid approximation techniques, one can provide an accurate starting point towards the development of this theory. Further, even this simplified model can make accurate statistical predictions about not only the experiments performed but real natural flows as well. The models developed further correct several misconceptions on the subject (such as the notion of a preferred wavelength in these systems) and, for the first time, allow a more detailed comparison between flows on eroding versus non-eroding surfaces, characterizing seemingly universal characteristics between them (such as Hacks' law [16]).

1.3 Previous Work

The subject of studying meandering streams has a long history. One can trace literature back to at least 1876 with a paper by J. Thompson, *On the windings of rivers in alluvial plains* [17]. The primary mechanism driving this meandering instability has been the subject of much controversy over the last 130 years and, under different settings, different conclusions have been drawn. Even A. Einstein wrote on the subject in 1926, speculating the earth's rotation may play an important role [18]. Initially, meandering was studied in natural settings such as river systems.

The uncanny visual similarities between river meanders and those observed on non-erosive substrates has drawn the community to attempt to make comparisons between these systems. However, the major conclusion drawn, previous to the current work, was that the mechanism for meandering on erosive substrates is the mobile-boundary, Seminara [19], while in the case of non-erosive surfaces the mechanism is surface tension, see [1], [13]. This creates a distinct difference for the underlying physics and hence comparison between systems has been limited.

Nonetheless, the rivulets became an active area of study through the 1980's [20],[21],[22], [23], [24], [25]. Many models for the non-erosive case were developed on these ideas, treating meandering as an intrinsic flow instability (see for example [1], [5], [14], [20], [26]). By creating models based on force-balance equations (between inertia, gravity, friction, surface tension, and centrifugal forces) linearization methods were employed to look at short time dynamics in an attempt to predict the dominant wavelength for this instability.

These models met with limited success and became quite difficult for further analysis. It is interesting to note that these models were generally built by using the river models previously developed, see [13], [27], [28], [29], but modifying them to include surface tension and neglect sediment transport.

In the late 1990's, a largely unnoticed work appeared by Nakagawa [30] by which experimental evidence of stable flow patterns was found to exist in a region of space
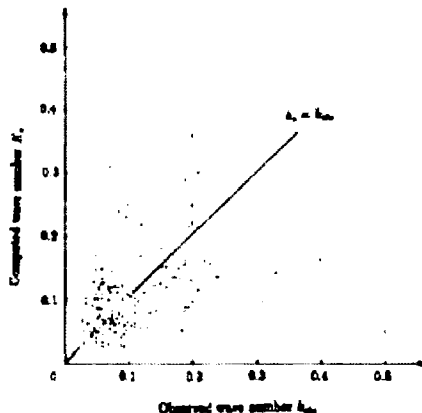
Figure 1.2: Previous prediction on initial wavelength of instability theory vs experiment. x-axis observed wavelength y-axis predicted wavelength (from Mizumura 1997 [1])

previously thought to be unstable. Later in 2004, analytic results for rivulets were published putting into further doubt the truth about when these flows were (and were not) actually stable to the meandering instability [12]. In 2006, further complexity was discovered by Le-Grand Piteira *et. al.* [5] where an experimental bifurcation diagram was presented showing transitions between stable flows, pinned meandering flows (meandering profiles not longer changing in time), and dynamic meandering flows (see Figure 6.1). Le-Grand Piteira *et. al.* began to address an additional flow structure where dynamic meandering gets pinned and becomes time independent. In Section 6.2, this specific point will be addressed in greater detail.

1.4 Initial Results on Stationary States

In 2002, the work of this thesis began as an experimental study to determine the governing parameters which control meandering instabilities. In particular, even before the knowledge of the work of Nakawaga *et. al.* [30], there were suspicions that certain flows could be made stable and straight if careful enough. A series of experiments were designed to observe the behavior in the immediate downstream
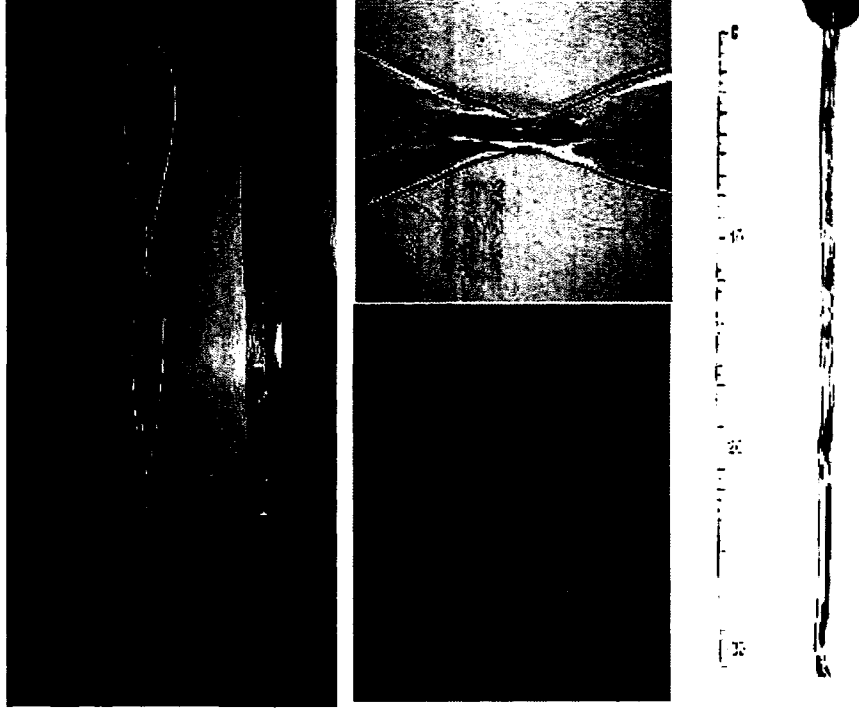
Figure 1.3: Braids and Rivulets (left to right)

flow of water (and water-glycerin mixtures) on flat acrylic plates under the influence of gravity. The choice of acrylic was based primarily on its availability, cost, and desirable surface properties. Acrylic is a partially wetting surface with a contact angle of roughly 57 degrees. As the contact angle is a measure of the surface-fluid interaction, this choice gives a moderately interacting surface. The experimental study was conducted across the parameter range shown in Table 1.1.

The experimental apparatus is extremely simple and a schematic is found in Figure 2.2. The essential factors found to control meandering for this setup are fluctuations in the flow rate and contamination and/or irregularities on the surface. The primary difference separating this apparatus from those in previous work is the use of a tall upper reservoir which, through the use of overflow valves at certain heights, ensures a constant hydrostatic pressure at the nozzle outlet. When the primary instability-causing mechanisms are removed, a stationary state is then observed. The details of the experimental setup are outlined carefully in Chapter 2.

System Parameter		
variable		Experimental Range
Inclination Angle	α	15-60 degrees from horizontal
Flow Rate	Q	100 ml-2 L/min
Kinematic Viscosity	ν	1-5 centistokes
fixed		Value
Fluid Density	ρ	1 g/ml
Contact Angle	θ	50 degrees
Surface Tension Coefficient	γ	70 dynes/cm

Table 1.1: System Parameters

It is important to note that even under ideal circumstances a transient stabilization time is always observed and can be substantial depending on the parameter choices and length of stabilization desired. For smaller flow rates, as well as increased viscosity, these transient times could be order of hours.

At least one other paper does claim to use a constant hydrostatic pressure to prescribed flow [3]. It is unclear why they did not see the flow restabalize. The authors explicitly mention the use of a rotameter- it is possible this induced enough flow rate variation to explain their observations. Perhaps, they only collected data for a few hours after turning on the apparatus. In which case, for a long incline they may not have waited long enough to get through the transient. Perhaps, the aspect ratio $A = \frac{H}{D}$ (where H is the fluid height in the upper reservoir and D is the diameter of the fluid jet) was too small and, therefore, there were still perturbations in the flow.

For constant flow rates, after the transient time passes, two distinct steady state flow patterns were shown to be present. A rivulet regime where the mean downstream velocity is roughly constant and the edges of the stream remain straight, and a braiding regime where the mean downstream velocity is non-constant and the edges of the stream experience decaying oscillation as progressing downstream (see Figure 1.3 and Figure 1.4).

1.5 Braids and Rivulets
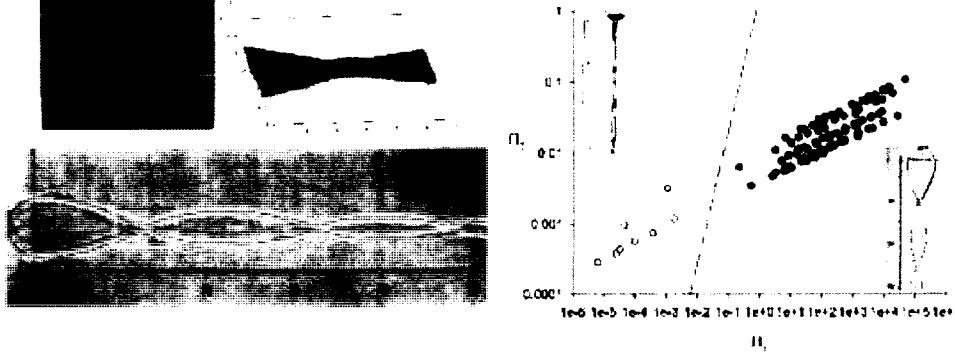
Figure 1.4: JPG overlayed with solution to equations (1.1 , 1.2)(left bottom); Recreation of free surface profile (left top); Bifurcation diagram (right)

The model for this steady state system was constructed from the boundary layer approximation of the Navier-Stokes equations parallel to the plane. After some approximations, the system could be reduced to a pair of ordinary differential equations for the stream width and the average down stream velocity at each cross-section.

$$(u \cdot w')' = F(u, w) - \pi_1 u^2 w^2 w' \tag{1.1}$$

$$u \cdot u' = 1 - \pi_2 u^3 w^2 \tag{1.2}$$

where

$$\Pi_1 = \frac{3Q\rho^2 \nu(gsin(\alpha))}{\gamma^2} \tag{1.3}$$

$$\Pi_2 = \frac{3Q^5 \rho^7 \nu(gsin(\alpha)^4)}{\gamma^7} . \tag{1.4}$$

With the use of averaging techniques [31], lubrication approximation, and a fourth order polynomial approximation for the free surface profile this model is able to explain this physics of this phenomenon from first principles, incorporating surface tension and inertia under the influence of gravity. For a more detailed construction of

this model and explanation of all analysis summarized here, see Appendix A and/or [7],[8] [32].

The physics of this phenomenon can be explained as follows: Braids are, in fact, decaying oscillation as the bulk of the fluid (traveling at the edges of the flow and separated by a thin film in between) are drawn together by surface tension and then bounce with decaying amplitude due to inertia, while driven by gravity. The model is able to predict the decaying oscillation as well as the free surface. Further, this model has the ability to explain the transition between the two distinct steady states (See Figure 1.4).

Conducting a linearization around the constant mean downstream velocity and constant stream width, one arrives at a cubic polynomial for the associated eigenvalue equation which can predict the bifurcation between flow regimes. This can be understood mathematically as a transition from one negative real, and two complex conjugate eigenvalues (braids) to three negative real eigenvalues (rivulets). The bifurcation diagram is in terms of two dimensionless groups constructed from the five dimensional parameters and the dimensionless inclination angle θ of this system.

Because the bifurcation line represents the limit as the imaginary part of the eigenvalues goes to zero (*i.e.* the wavelength goes to infinity), this implies distinguishing data near the line is impossible (*i.e.* it is hard to tell a straight stream from one with an almost infinitely long wavelength). Nonetheless, for parameter values which are clearly on either side of this line, it is in excellent agreement with the experimental observations.

Now that the existence is established, and physics understood, for the stationary states a solid foundation is laid, both experimentally and theoretically, to begin a detailed study of meandering on non-erosive partially wetting surfaces.

SECTION II.

An excerpt from *On the cause and characteristic scales of meandering and braiding in rivers* [13] representing the fundamental philosophy on meandering which has influenced *most* work in the area of stream meandering.

> *The thesis that meandering is an inherent property of the flow, and that sediment transport is necessary only in a kinematic way to impose flow pattern on the bed, must be discarded in so far as present theories applies. Rather, it is indicated that the existence of sediment transport is a dynamically necessary condition for the formation of instability leading to meandering either in the flow or on the bed. This conclusion must be reconciled with the fact that meandering in fluid streams occurs in circumstances in which sediment transport is not present; namely in oceanic currents such as the gulf stream, streams of meltwater on ice, and Gorycki's streams a few milliliters wide on plastic plates. Common to all meandering streams are potential (inertial and gravitational) and friction effects; it is proposed here that an additional 'third effect' is required for meandering. This third effect is as follows: for alluvial streams, sediment transport; for oceanic currents, Coriolis acceleration; for glacial meltwater streams, heat difference, and for Gorycki's streams, surface tension.*
> *Parker 1976*

Chapter 2

Experimental Investigations

2.1 Meandering

Figure 2.1: Experimental Meandering (left); River Meandering (right)[2]

Meandering in nature is obviously far more complex than in the lab due to the extreme turbulence in rivers, erosion and transport of the underlying landscape, flooding, anthropogenic influences, *etc.* Modeling river meandering has been an

active area of research among geomorphologists for many years [13], [27], [28], [29], [33], [34], [35], [36], [37], [38], [39] as just a few examples. In fact, one can find more than ninety publications in the Civil Engineering Database alone since 1990 [40]. On the other side of this problem, more and more papers began to accumulate investigating non-erosive surfaces [3], [14], [20]. However, no one knew how accurately any comparison could be performed between these two different systems. Further, the types of questions they were trying to answer in their various settings were not suggestive of anything that could or should be quantitatively compared. No one knew exactly how the erosion was influencing the behavior compared to what they witnessed. It is clear that erosion and sediment transport must influence the flow behavior, but how?

While this is an interesting question, which will be addressed in this work, the discussion will be postponed until the end of Chapter 3. For the remainder of Chapter 2 and the primary portion of Chapter 3 this thesis will focus on understanding meandering on non-erosive partially wetting surfaces such as acrylic and polypropylene.

Due to the overwhelming complexity of this system, initially a set of goals was set for the current research. These points serve as the motivation for the remainder of Section 2.

1. Identify the mechanism for sustained meandering.

2. Measure the spectrum and investigate the existence of a preferred wavelength.

3. Generalize the stationary state model to understand meandering statistics.

4. Investigate any connections these flows share with those observed in nature.
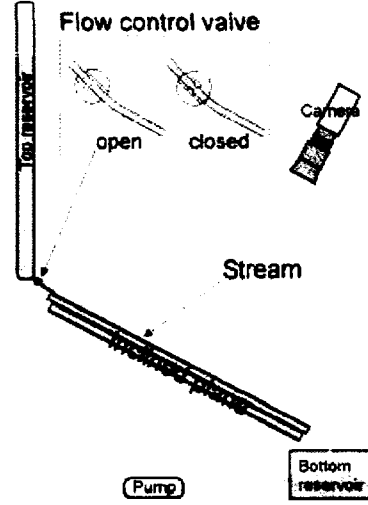
Figure 2.2: Schematic of Experiment

2.2   The Experimental Setup

The experimental arrangement (Figure 2.2) provides a highly constant discharge rate from a tall cylindrical top reservoir through a hole in its bottom connected to a flexible plastic tube. The diameter of this tube, and the hole, is $d = 3$ mm. The diameter of the container is $D = 15$ cm. Thus $d \ll D$, and the flow discharge rate Q is fairly well approximated by the formula originally introduced by Torricelli, $Q = \frac{\pi d^2}{4D^4}\sqrt{2gZ}$, where g is acceleration due to gravity and Z is the height differential between the location of the hole and the free surface [41] . Thus, if Z remains constant, Q is constant as well. For a fixed tube diameter, Q can be altered by changing Z.

The flexible tube that carries the flow to the inclined plane is necessary to prevent any capillary instabilities that might form on the free surface of a water jet. The jet was introduced onto the plane in two different ways:

- Perpendicular to the plane at a constant height of ~ 1 cm.

- Parallel to the plane.

17

Meandering System Parameter		
variable		Experimental Range
Inclination Angle	α	30,45 degrees
Contact Angle	θ	57 ± 2, 74 ± 5, 99 ± 4
Flow Rate	Q	3 flow rates used see Table 2.2
Kinematic Viscosity	ν	pure water, 50-50 water/glycerin mixture
pulse rate		1/3pps, 1pps, 4pps; with duration of order milisec.

Table 2.1: Meandering Data Collected

An electronically controlled valve, which could alter the flow rate by squeezing the tube, was also introduced upstream of the discharge point. Initially, several amplitudes of the pulse were investigated, for several types of signals, at various frequencies. For all amplitudes inspected (between roughly 10 and 100 percent reduction), meandering was a persistent feature of the flow. Hence, all data collected for analysis use a fixed amplitude of volume contraction ("strength of squeeze"). Ranges can be found in Table 2.1 and Table 2.2. The inclined plane is produced by placing a large (2.4 m long and 1.2 m wide) sheet of acrylic plastic (3.2 mm thick) on top of a 2.4 m

Flow Values Investigated for Meandering	WATER	50-50MIX
w/o pulses		
FLOW 1	187.5ml/min	100ml/min
FLOW 2	315.8ml/min	171.4ml/min
FLOW 3	428.6ml/min	222.2ml/min
w/ .37 pulse/sec		
FLOW 1	181.2ml/min	92.3ml/min
FLOW 2	272.7ml/min	150ml/min
FLOW 3	375ml/min	214.2ml/min
w/ 1 pulse/sec		
FLOW 1	176.5ml/min	85.8ml/min
FLOW 2	271ml/min	143ml/min
FLOW 3	333ml/min	200ml/min
w/ 4 pulses/sec		
FLOW 1	50ml/min	38ml/min
FLOW 2	105ml/min	65ml/min
FLOW 3	157.9ml/38sec	94ml/min

Table 2.2: Meandering Flow Data Collected

$\times$ 1.2 m $\times$ 2.5 cm urethane slab, which in turn is mounted on a welded-steel frame. This frame is attached to two pivots with a screw arrangement controlling its angle of incline α with respect to the horizontal.

After the flow exits the tube, it runs down the incline and into a long rectangular bottom reservoir, from which it is recirculated with an electric pump connected to the top reservoir. Note that the top and bottom reservoirs are also connected with an overflow tube, which ensures that the free surface of the top reservoir remains at a constant level. The stream of fluid in this setup is highly controllable.

After some initial settling time, the stream flowing down the plane assumes a straight shape for all the flow regimes investigated. During the settling time, three distinct flow regimes could be observed (see Figure 2.5):

- First, a region in the immediate downstream where stabilization had occurred,

- Second, a region of continuous meandering,

- Third, a region where the stream breaks up.

In the third regime, stream splitting events usually occur at the inflection points of the stream.

If the flow control valve remains open (no flow rate disturbances), the stream always stabilizes to the stationary non-meandering shape. Note that the long and narrow top reservoir stabilizing the flow is crucial for rivulet stabilization. If that reservoir is removed, or a flat and shallow reservoir is used (even having the same volume capacity), the meandering never stops due to the inherent disturbances introduced by the pump. Thus, careful attention to disturbances in the flow is imperative for this experiment.
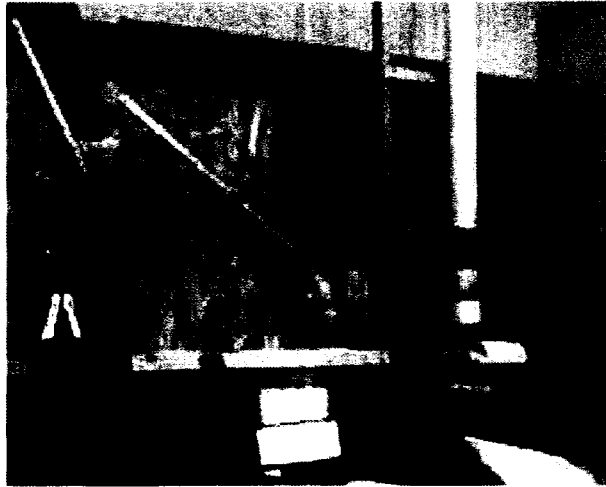
Figure 2.3: Experiment used to inspect various perturbations to steady state flows

2.3 Experimental Stability

Having knowledge of the steady state flows, the next obvious question is, how robust are the stationary states to perturbation? The initial expectation was that flow stability should be extremely sensitive to any perturbation, after all these stationary states are almost never seen in nature. To be cautious of this possibility, the initial perturbations were done using a three-inch speaker held fixed approximately two inches above the plane immediately downstream of the nozzle. The tone was created using a sine wave generator and a pre-amp allowing variable power of up to roughly 10 watts continuously. The range of frequencies investigated spanned from 0-4000kHz continuously. The results in all cases were similar. While the given perturbation may induce a temporary meandering state, the flow would always re-stabilize under the influence of any constant signal.

The second set of experiments were then conducted by attaching the nozzle itself to a linear oscillator which was capable of introducing oscillations perpendicular to the flow direction ranging from 0.5cm to 5 cm discretely with frequencies less than 100 Hz continuously (see Figure 2.3). Note that when running at maximum capacity, the accuracy and linearity was very uncontrolled. It was more like a chaotic pendulum. Nonetheless, even under these extreme circumstances, stabilization was

Chapter 2. Experimental Investigations

observed. The conclusion of these experiments demonstrated that if a perturbation had time to be quenched by the downstream flow, then the flow would re-stabilize. Hence, only perturbations capable of traveling upstream could sustain meandering.

The third set of experiments was then conducted using perturbations in the form of shocks, which are then capable of upstream travel. By a slight modification to the previous schematic, which is shown in Figure 2.2, namely inserting an electronic valve into the system which introduces controllable flow rate fluctuations, pulses to the flow could be introduced in a controlled way. This type of perturbation was found to lead to the immediate onset of indefinite meandering. Amazingly, even a small pulsation of this type is capable of sustaining meandering (tests ran for up to twenty-four hours). In a few instances, the meandering would seem to become stationary. However, in this experiment the cause was always attributed to surface contamination. While there may actually be something more complex happening here, one can say with certainty that cleaning the surface and restarting under the same conditions would not generate consistent pinned patterns. As the range of parameters investigated is well within the dynamic range given by Le Grande-Piteira *et. al.* [5](see Figure 2.3) this does not necessarily contradict the existence of stationary meandering for small flow rates. For small flow rates the effects of surface interactions become much more dominant and pinning does not seem unreasonable.

For the entire parameter range investigated, switching on the pulses prompted almost immediate meandering. Switching off the pulses would yield stationary states after a transition period. While the transient meandering time may be on the order of several hours for slower flows, patience would always yield steady state flows the complete length of the acrylic sheet. For the meandering analysis conducted, several measurements were made varying surface contact angle, flow rate, pulsation rate, inclination angle, and viscosity. For the range of values studied, see Table 2.1 and Table 2.2. Additionally Figure 2.4 shows the static contact angle for the three surfaces studied. Note that all the meandering data collected was under the influence of constant pulsation.

21

Figure 2.4: Contact angles for various surfaces studied, Acrylic, Coated Acrylic, Polypropylene (left to right)

2.4 Meandering Regimes
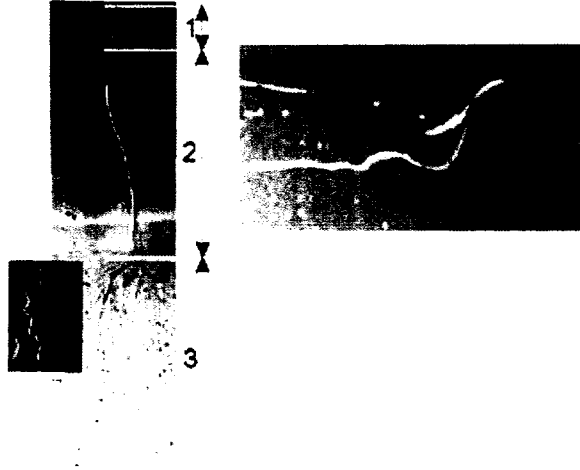
Figure 2.5: Three Regimes (left); Splitting (right)

Through the work of this thesis, it has been shown that at any instant in time during the transient period of flow stabilization, there are three distinct regimes as a fluid flows down an incline plane (see Figure 2.5). Based on the choice of parameter values, one can adjust the size of these various regimes as desired. For a flow which is given all the necessary conditions for stability, one can follow the transition points between these regimes as they move down the plane. In the immediate downstream, the flow will become stable fairly quickly. At some point downstream a "tail" will appear where the stream begins to meander. Initially, the meandering stream will stay coherent and therefore there will exist a second regime for which the stream will

22

remain continuous as it writhes back and forth across the plane.

Still further down the stream one will then observe a second point at which the stream will split, sometimes breaking into two streams other times into several. At this point the behavior becomes completely chaotic and is beyond the focus of the current work. While it has not been theoretically addressed, experimentally one seemed to observe a statistically regular velocity of these two transition points during stabilization. There is additional data collect for analysis of this behavior when time permits in the future.

The present work only accounts for analysis of data under the influence of pulsation. By increasing the viscosity in these flows, one can increase the size of the continuous meandering regime to the full extent of the acrylic plane used. By this method the current work was therefore able to obtain stream lengths long enough to begin consideration of statistical work.

2.5 Splitting Regime

Before leaving the topic of stream splitting and the third regime, a few important remarks concerning experimental observations should be addressed. A stream splitting event in the lab will almost always occur as a consequence of one of two events, either; As the meandering stream fans across the plane it requires the flow further downstream to move faster and faster to "keep up". Eventually, at some distance downstream, this is impossible due to friction and the stream slides off itself. More typically one observes a "buckling" occur where a cusp forms at an inflection point of the stream.

A paper has been published studying this third regime Schmuki *et. al.* [3] and this phenomena has been clearly connected to contact angle hysteresis. By studying the number of splitting events that occurred per unit time at each cross-section the authors were able to explain, using energy considerations, the scaling law observed which were in good agreement with their theory (see Figure 2.6).
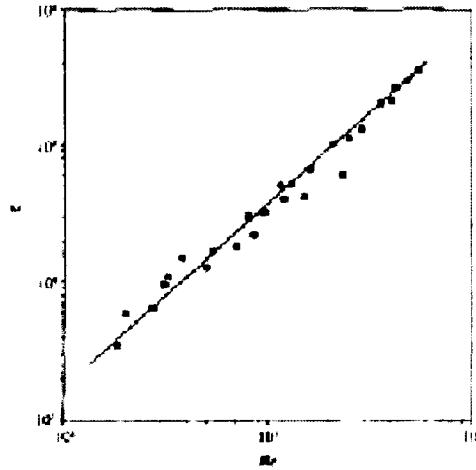
Figure 2.6: Theory vs experiment for prediction of splitting events based on energy considerations Schmuki *et. al.* 1994 [3]

2.6 Data Analysis
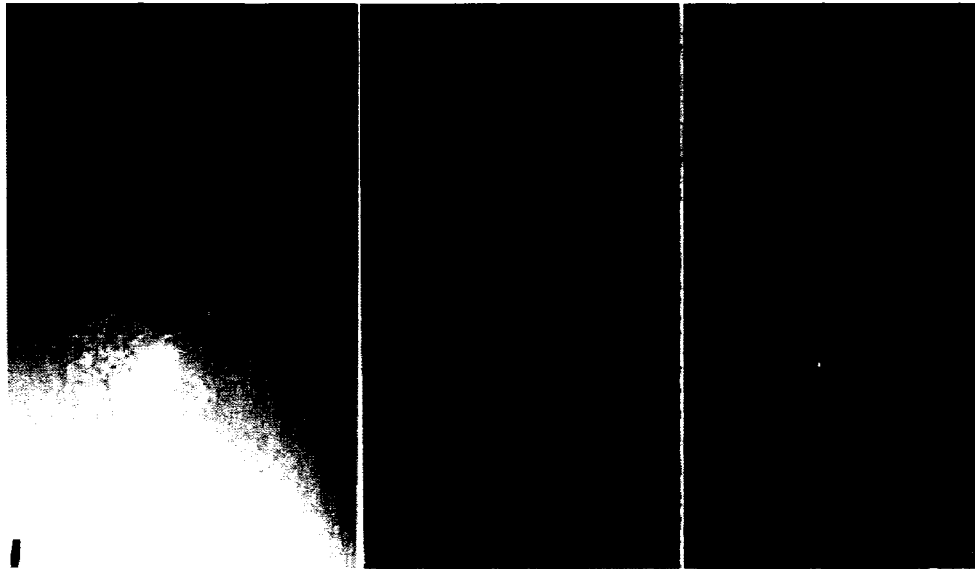
Figure 2.7: Typical digital image acquired through experiment, grey-scaled and undistorted, stream center line found (in black) and overlayed on original jpg image (left to right)

Figure 2.7 shows a typical image obtained in experiment. These images are

24

captured with a 4-megapixel grayscale digital camera mounted above the incline. The effective resolution of the images is about 1 mm per pixel. Any optical distortions are removed from these images as follows: An image of a rectangular grid is captured by the camera. This bitmapped image with any distortions is then mapped to the bitmap containing the undistorted image. The mapping procedure produces a bicubic spline mapping scheme which is then used to process the experimental images. Prior to each experimental run, a background image with no stream is captured, to be subtracted from the images showing the stream and the droplets left in the process of its meandering. Subsequently, the image is grey-scaled [42] and then, with the use of a Matlab code, the centerline of the stream is extracted from the processed images. The conservative estimate of the cumulative error of the extraction and distortion correction for the centerline coordinates is on the order of one pixel (about 20% of the characteristic stream width).

The stream centerline profiles were then compiled into a list. After conducting experiments across the parameter space indicated in Tables 2 and 3, about 200 images were accumulated. Analysis was then done to look at ensemble average spectrum for various subsets of this data. It is important to note each image was taken at least 5-10 minutes after the stream profile began to develop. The focus of this work is on fully developed stream profiles. Further, all images were taken far enough apart in time to be considered statistically independent. The results for each surface are plotted in Figure 2.8. A rescaled comparison is also plotted along with theory in Chapter 4.

In addition to doing data analysis on the stream profiles themselves, it was also found that work would need to be performed to understand the distributions of droplets left by the stream on the plane. As a stream meanders, it leaves a thin film in its wake, which almost immediately breaks up into droplets. These droplets are then left to be later re-encountered by the stream. In Chapter 4 the inclusion of this effect must be addressed to obtain a physically reasonable model. In this section some of the basic information about these droplets is included.

Each image was resolved using Imagetool ©[43] and a random sample size of
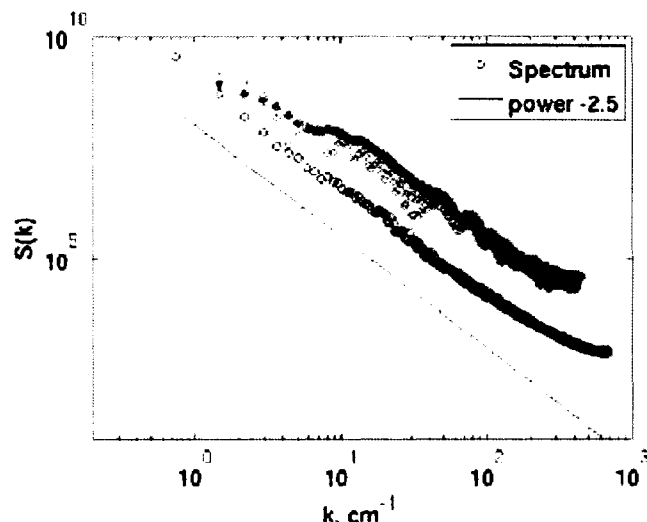
Figure 2.8: Unscaled Spectra (Green=acrylic,Red=RainX,Blue=Polypropylene)

roughly 10,000 droplets. First, note that while the scaling of the spectra remains similar for all surfaces investigated (Figure 2.8), the amplitude does change. This is the first indication that there are still differences between the flows found on varying surfaces. In fact, observation shows that as the interaction with surface increases (*i.e.* contact angle decreases), the meandering increases in amplitude of deviation and the meanders themselves move slower. One can then ask to what extent is this behavior explained by these droplets?

Analysis of these distributions shows that, as one may expect, they are not identical for all surfaces. Inspection of Figure (2.9) shows size distributions for the various surfaces and also the growth rate of deviation. The growth rate seems to be a function of the contact angle (*i.e.* increasing contact angle decreases the number of droplets and the growth rate of deviation of the streams center line).

Unfortunately, there is insufficient data to feel confident looking at these deviations too far from downstream. Further work should include the collection of a much larger data set for study of such questions. Nonetheless, it gives the basic idea that the issues of contact angle are still looming in this problem.
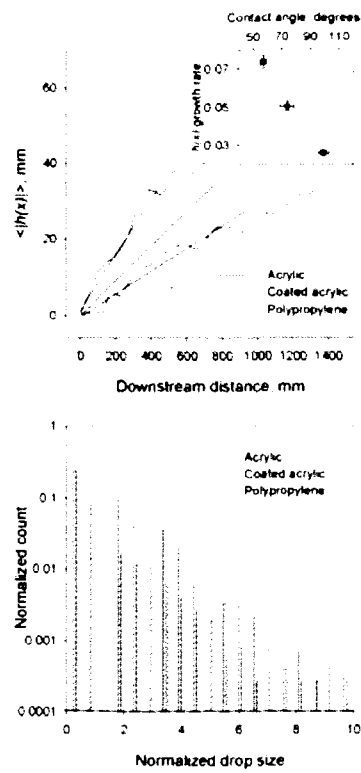
Figure 2.9: Top: Growth rates of $\langle |h| \rangle$ vs downstream distance for various surfaces; Top Insert: Growth rates vs contact angle; Below: Distribution of drop sizes for various surfaces

Chapter 3

Theoretical Model

3.1 General Considerations

Using the previous knowledge about the steady states it is fair to assume the same basic processes must be accounted for in the force balance equations. Hence, one should expect the influences of gravity, surface tension, friction, and inertia to be important. However, by inspection of Figure 2.7 (and as was addressed in the previous section) one can see that when a fluid stream meanders on a partially wetting surface, another contribution becomes apparent. That is, as the fluid writhes back and forth across the plane it leaves a thin film in its wake which almost immediately breaks up into droplets. These droplets are then left to be later re-encountered by the stream. Upon this collision each droplet acts as an additional local transverse forcing mechanism on the stream. Therefore a model cannot be correct without explicitly taking this into account.

3.2 Starting with Navier-Stokes Equations

$$\frac{d\mathbf{U}}{dt} + \mathbf{U}\nabla\mathbf{U} = \frac{1}{\rho}\nabla\mathrm{P} + \mathrm{g}\sin(\alpha)\hat{\mathbf{e}}_x + \nu\nabla^2\mathbf{U} \tag{3.1}$$

As with the stationary state model, the model again starts from (3.1) and the in-compressibility condition (See Appendix A). Now, however, the previous technique of approximating the free surface profile becomes much more challenging. Without an explicit function to characterize the free surface profile, the calculation of pressure (surface tension) term in 3.1 will have to be done using variational Calculus.

Additionally, the influence of the droplets makes this problem stochastic. That is, until it is possible to predict the exact size and location of each droplet as a function of time, the best one can do is with the use of distribution functions. Obviously, the ability to predict these drops from first principles is a challenging problem and currently there is no complete theory for how to achieve this in even the simplest settings. For the current purposes, the use of stochastic modeling will not be a serious limitation.

3.3 Surface Tension
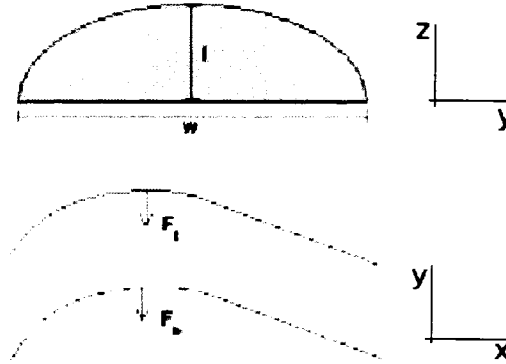
Figure 3.1: Top: Fluid cross-section in yz plane; Bottom: Fluid cross-section in xy plane demonstrating two curvatures present

Chapter 3. Theoretical Model

For the arbitrary stream volume element, there are two curvatures which must be considered when contemplating surface tension. See Figure (3.1). There is the curvature in the xy plane and that in the yz plane. Initially, for simplicity, consider only the curvature in the xy plane. To perform this calculation, approximate the cross sectional area in the yz plane by $A = lw$ where l is the average stream height and w is the average stream width. It is clear that this is an approximation. In Section 3.5, it will be addressed when this approximation is most valid. Further, in Section 6.1, how one could do better will be discussed, along with the difficulties encountered. For now, this choice will greatly simplify analysis and under this approximation it will still be possible to gain many insights into this problem.

To calculate the surface tension force in the xy plane, consider the use of variational methods. The basic procedure will be relied on twice in this manuscript and therefore an outline of how to calculate variational derivatives is found in the Appendix.

By considering the functional, which represents energy per unit arclength

$$E = \gamma w \int_{x_1}^{x_2} \sqrt{1 + h_x^2}\, dx \;,$$

the force/volume, due to curvature differences on the top and bottom edges of the stream, can then be found as roughly:

$$\frac{1}{A}(F_t - F_b)dx = \frac{1}{A}\frac{\delta E}{\delta h} = -\frac{\gamma}{l}\frac{\partial}{\partial x}\left(\frac{h_x}{\sqrt{1 + h_x^2}}\right) \;.$$

Here, the relation $A = wl$ has been used. Also, γ is the coefficient of surface tension, and the subscripts t and b are the force felt by the top and bottom respectively as shown in Figure 3.1.

3.4 Colored Noise

An important part of the subsequent discussion is the structure of the noise. There are two possibilities. First, one can take $\eta(x, t)$ as a white noise with the correlation $\langle \eta(x,t)\eta(x',t')\rangle = A\delta(x-x', t-t')$. This assumption leads to an analytical solution (in a stochastic sense) for the system derived in Chapter 5 under the assumption that the friction coefficient λ vanishes in the equations of motion presented in Section 3.6. The solution, interestingly enough, provides a meandering exponent of 1/6 corresponding to real-world rivers. This solution is presented later in Chapter 5. However, assuming $\eta(x, t)$ to be white noise is not adequate for explanation of the experimental results. Indeed, the white noise ansatz for $\eta(x, t)$ can only be assumed if there is a large number of droplets of random sizes distributed all over the length of the meandering stream, and acting at all times. This assumption is correct for large-scale flows like rivers, where there *is* continuous random forcing on all scales.
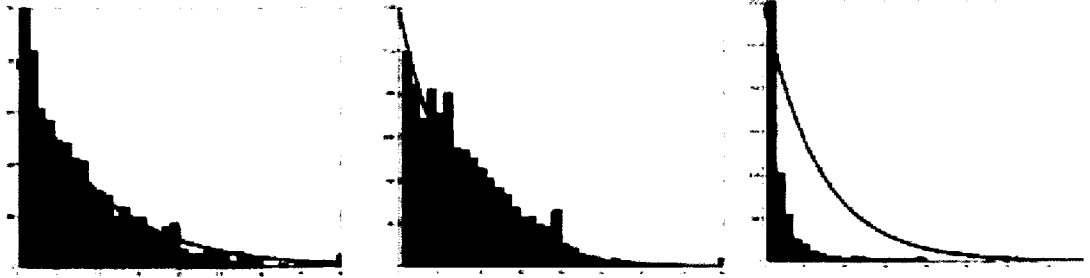
Figure 3.2: Drop size distributions for various surfaces studied: Acrylic, Coated Acrylic, Polypropylene (left to right).

When attempting to reconstruct droplet distributions, there are actually two types of distributions one might initially consider: those in size and in space. Figure 3.3 shows typical $25cm^2$ patches of droplets for the various surfaces studied. Analysis was performed to investigate size distributions as a function of surface contact angle. Figures 2.9 and 3.2 demonstrate that the choice of material does affect the distribution properties.

In this experiment, at each given time instant, the stream encounters only a very limited number of droplets. Thus, it is most reasonable to use the assumption that

31

Figure 3.3: 25 cm^2 sample patch of droplets for each surface (increasing contact angle left to right)

$\eta(x, t)$ is a spike appearing at a random sequence of times $t_1, ...t_n, ...$ At each time t_k, the position of the spike x_k is also chosen at random. Several types of distributions have been tried for these droplets in space, and as long as they are not too skewed (*i.e.* , concentrated towards the beginning or the end of the stream), the results do not change for wavelengths corresponding to the scales larger than droplet size. In addition, the results do not change depending on the shape of each droplet as long as it is localized. In particular, a rectangular pulse function of width l, inverse Helmholtzian $exp(-|x - x_n|/l)$ and Gaussian $exp(-(x - x_n^2)/l^2)$ distribution type were used. Because the exact nature of the distribution was not critical, for the numerical results presented in Chapter 4, this function was approximated using the average drop size for each surface and a uniform distribution in space. This allowed the reduction to a single fitting parameter for the average force felt by the moving contact line each time it encountered a droplet.

Hence, the nature of the noise in this problem is "colored" in that it is highly concentrated at a particular scale and localized. Note that all the modeling results presented here assume uniform distribution of droplet times $t_1, ...t_n$; for each time t_k the distribution of droplets x_k is uniform in space. The shape of the forcing is Gaussian, with width l equal to the cross-section of the stream (2 mm).

3.5   Equations of Motion

Consider the flow of fluid on an inclined plane at an angle α with the horizontal. Define the (x, y) Cartesian coordinate system in this plane so that its origin coincides with the origin of the stream, and the x axis is pointing straight downstream (*i.e.1*, the centerline of a non-meandering rivulet will follow the x axis). Then the momentum equation for the fluid in the rivulet can be written as

$$\frac{d\mathbf{U}}{dt} + \mathbf{U}\nabla\mathbf{U} = \frac{1}{\rho}\nabla\mathrm{P} + \mathrm{g}\sin(\alpha)\hat{\mathrm{e}}_{\mathrm{x}} + \nu\nabla^2\mathbf{U} + \mathbf{H}\ .$$

The dominant contributions to the force balance come from the surface tension, friction on the bottom of the stream, and internal viscous dissipation, all of which work against fluid inertia and gravity.

3.5.1   Lubrication Approximation for Frictional Force

Here, consider a lubrication approximation to reduce the full three-dimensional equations with boundary conditions (z axis being normal to the plane of the flow) to equations in two dimensions where the z dependence is averaged out and the no-slip condition on the bottom is implicitly accounted for. A very similar technique has been described in detail in Appendix A. The lubrication approximation is based on the assumption that the vertical velocity profile in the fluid is parabolic due to the non-slip boundary condition on the bottom of the stream and the stress-free condition on the top (free surface).

With these assumptions, one can show the x component of the friction force to be $F_{f,x} = 3\nu u/l^2$, where u is the value of the x component of velocity averaged in the z direction and, as before, l is the average stream depth. As the stream is narrow, one can safely assume that u does not vary much in the cross-stream direction.

Similar parabolic-like velocity profile is expected in the cross-stream (y) direction with velocity vanishing at the contact lines (similar to theoretical results of Perazzo

et. al. [12]). The cross-stream dependence on y over the width w can then also be averaged out. The total friction terms in this direction are then $F_{f,x} = -3\nu u(1/l^2 + 1/w^2) = \lambda u$. Thus, introduce single values of the velocity components $U = ue_x + ve_y$ in the x- and y- directions for a given cross-section of the stream. Let the stream
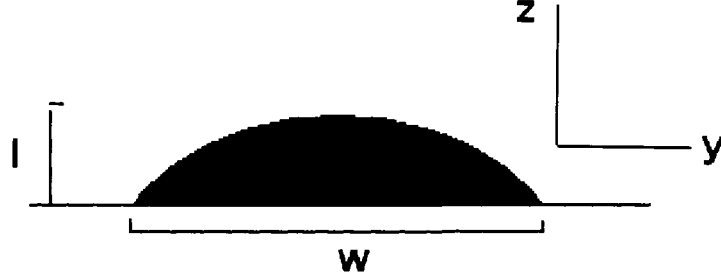
Figure 3.4: Schematic of cross-section in yz-plane, demonstration connection between l w and θ

discharge rate at a given location be $Q = Au$, where A is the cross-sectional area of the stream in the plane normal to the x-axis. Assume that the width of the stream is w. The area of this section is $A = lw$. Now, using $Q = Au = lwu$, write the equation for the friction force as $F_{f,x} = 3\frac{\nu u^2 w}{Ql}(1 + \frac{l^2}{w^2})$.

The simplest possible form of the equation describing the free surface ξ in this plane is parabolic, $\xi = \frac{3}{2}l(1 - \frac{4y^2}{w^2})$. The ratio w/l is actually related to the contact angle θ as follows. By evaluating $\frac{\partial \xi}{\partial y}$ at $y = w/2$ (the edge of the stream), one finds the value to be $6l/w$. But this slope equals $\tan\theta$. Thus $w/l = 6/\tan\theta$.

This implies $F_{f,x} = -\frac{18\nu u^2}{Q\tan\theta}(1 + (\frac{\tan\theta}{6})^2)$.By introducing a parameter $\lambda = 18\nu(1 + l^2/w^2)/(Q\tan\theta) = 18\nu(1 + (\tan\theta/6)^2)/(Q\tan\theta) \approx 18\nu/(Q\tan\theta)$ and performing similar analysis for the y-component of the friction force, one can then write the

following expressions for the components of the friction force in the two-dimensional formulation of the problem: $F_{f,x} = -\lambda u^2$ and $F_{f,y} = -\lambda uv$.

3.5.2 Equations of Motion: First-Form

Consider the pressure term, with the pressure to be inferred from the influence of surface tension. For this derivation, assume that the variation of the width of the stream $w(x,t)$ is sufficiently small that the width can be represented by its characteristic value w. In reality, the shape of the cross-sectional area of the stream changes with time, and the contact angle is subject to hysteresis. However, if one is dealing with gradual movement of the stream (characteristic contact-line velocities associated with meandering are much lower than $U = |U|$), it is reasonable to assume that the variation of this shape is commensurately small, and so are the variations of w and l. For this, and the subsequent derivations, also regard the downstream velocity components as uniquely defined by the downstream distance x, as all the variations of velocity in the cross-section of the stream are either small enough to be irrelevant (in the y direction) or have been averaged out (in the z direction).

Let the deviation of the centerline of the stream from the x-axis be $h(x,t)$. For a straight rivulet, $h(x,t) = 0$. Then the length of the centerline of the stream between downstream locations x_1 and x_2 is $L = \int_{x_1}^{x_2} \sqrt{1 + h_x^2} dx$, where $h_x = \frac{\partial h}{\partial x}$. For a contact angle characterizing a partially wetting surface ($\theta < 90$), the stream is shallow ($l = \frac{w \tan(\theta)}{6}$). Thus the surface area of the stream between x_1 and x_2 is approximately the same as the wetted area

$$S = wL = w \int_{x_1}^{x_2} \sqrt{1 + h_x^2} dx .$$

The surface tension will tend to minimize this surface area, thus the surface tension force per unit length is $F_s = \gamma \frac{\delta S}{\delta h}$. Thus, the corresponding capillary force per unit volume is

$$\frac{1}{A}(F_t - F_b)dx = \frac{1}{A}\frac{\delta E}{\delta h} = -\frac{\gamma}{l}\frac{\partial}{\partial x}\left(\frac{h_x}{\sqrt{1 + h_x^2}}\right)$$

as was derived previously in Section 3.3. The component form of the equations of motion then take the form:

$$\frac{\partial u}{\partial t} + u\frac{\partial u}{\partial x} = g\sin(\alpha) - \lambda u^2 + \nu\frac{\partial^2 u}{\partial x^2} + \frac{1}{A\rho}\frac{\delta S}{\delta h}\cos\psi + \eta_x \tag{3.2}$$

$$\frac{\partial v}{\partial t} + u\frac{\partial v}{\partial x} = -\lambda uv + \nu\frac{\partial^2 v}{\partial x^2} + \frac{1}{A\rho}\frac{\delta S}{\delta h}\sin\psi + \eta_y \tag{3.3}$$

$$\frac{\partial h}{\partial t} + u\frac{\partial h}{\partial x} = v \, . \tag{3.4}$$

The terms containing λ are added as the result of the use of a lubrication approximation. Angle ψ in the terms representing the components of the pressure (*i.e.* , surface tension) force is the angle between the direction of the stream and the x-axis, in other words, $\tan\psi = h_x$. The components of the random force **H** are $\eta_x = \eta\cos\psi$ and $\eta_y = \eta\sin\psi$. The third equation is a kinematic condition for $h(x,t)$.

3.6 First Rescaling

The system (3.4) can be further simplified by considering rescaling under the assumption that $v \ll u$. Then, $h_x \ll 1$ and the surface tension term linearizes as follows:

$$\frac{\delta S}{\delta h} = -\frac{h_{xx}}{\sqrt{1 + h_x^2}} \approx -h_{xx}$$

this reduces the system to

$$\frac{\partial u}{\partial t} + u\frac{\partial u}{\partial x} = g\sin(\alpha) - \lambda u^2 + \nu\frac{\partial^2 u}{\partial x^2} + \eta_x \tag{3.5}$$

$$\frac{\partial v}{\partial t} + u\frac{\partial v}{\partial x} = -\lambda uv + \nu\frac{\partial^2 v}{\partial x^2} + \frac{\gamma}{\rho l}\frac{\partial^2 h}{\partial x^2} + \eta_y \tag{3.6}$$

$$\frac{\partial h}{\partial t} + u\frac{\partial h}{\partial x} = v \, . \tag{3.7}$$

Chapter 3. Theoretical Model

This model is therefore accurate to order $\sim O(h_x^2)$. All numerical analysis performed in Chapter 4 will use this set of equations. Notice at this point that the u equation has decoupled, while the remaining two equations for v and h are now linear.

3.7 Stability Analysis

The following subsections address various stability calculations which can be performed on the set of equations derived in the previous section. Some additional notes about conventions and notation can also be found in the appendix.

3.7.1 Linearization and Spatial Instabilities

With these equations one can now perform some standard linearization techniques to see what, if anything, can be said about the initial meandering instability. Consider

$$u_t + uu_x = g\cos\alpha + \nu u_{xx} - \frac{\lambda u^2}{Q} := \nu u_{xx} + F(u) \ .$$

Consider stationary solutions $u_t = 0$ about $F(u_*) = 0$ *i.e.* $F = 0 \Rightarrow$

$$u_* = \sqrt{\frac{Qg\cos\alpha}{\lambda}} \ .$$

Now, linearize about u_* by $u = u_* + \epsilon\tilde{u}$ dropping terms of order ϵ^2 and dropping $(\tilde{\ })$ notation one arrives at

$$u_{xx} - \frac{u_*}{\nu}u_x - \frac{2\lambda u_*}{Q\nu}u = 0$$

yielding the characteristic equation

$$\Gamma^2 - \frac{u_*}{\nu}\Gamma - \frac{2\lambda u_*}{Q\nu} = 0 \ .$$

This gives eigenvalues of

$$\Gamma = \frac{u_*}{2\nu} \pm \frac{1}{2}\sqrt{\frac{u_*^2}{\nu^2} + \frac{8\lambda u_*}{Q\nu}} \ .$$

This shows that the $Re(\Gamma) >$ implying it is unstable! What is worse is that this calculation carries over to the v equation in the same fashion. Consider

$$v_t + uv_x = -\frac{\lambda}{Q}uv + \nu v_{xx} + \frac{\gamma}{\rho l}h_{xx} \ .$$

coupled to

$$h_t + uh_x = v$$

but in the steady state $h = 0$, u roughly constant, and $v_t = 0$ so this becomes

$$v_{xx} - \frac{u}{\nu}v_x - \frac{\lambda u}{Q\nu}v = 0$$

leading to eigenvalues

$$\Gamma = \frac{u}{2\nu} \pm \frac{1}{2}\sqrt{\frac{u^2}{\nu^2} + \frac{4\lambda u}{Q\nu}} \ .$$

This result again suggests that the $Re(\Gamma) > 0$ implying it is also always unstable. Hence, these calculations can not be correct since they predict exponential growth for all values of constant flow, which is not what is seen in experiment! This will be attributed to limitations of linearization techniques. This point will become more apparent as the calculation proceeds.

3.7.2 Temporal Meandering Stability- Constant Flux

Now consider temporal stability of the u-equation. As has been seen previously, the coupling between u and v in h means when u is stable so is v and vice-verse. This happens explicitly because of the one-way coupling between the u and v equations, *i.e.* v is coupled to u, but not the reverse. Physically, this makes sense since the linearization is about a straight rivulet.

Consider

$$u_t + uu_x = g\cos\alpha + \nu u_{xx} - \frac{\lambda u^2}{Q} := \nu u_{xx} + F(u) .$$

Consider solutions about $F(u_*) = 0$ as before so the linearization becomes

$$u_t + u_* u_x = \nu u_{xx} - \frac{2\lambda u_*}{Q} u .$$

Then assuming solutions of the form $u(x,t) = a(t)e^{ikx}$ one arrives at

$$\hat{P}(ik) = -\nu k^2 - \frac{2\lambda u_*}{Q} - iu_* k .$$

Because $\hat{P}(ik) < 0$ for all k, implying for constant Q the flow should be stable. This is a good result, and in agreement with observation, if the flux Q is constant, the flow is stable. However, to justify the claims that: 1. Flow rate perturbations cause the onset of meandering and 2. Noise is responsible for the amplification and sustainability, more is needed still.

3.7.3 Temporal Meandering Stability-Varying Flux with Constant Amplitude I

Now, consider linearization of the u equation including fluctuations in Q (initially with constant amplitude) such that $Q = Q_0(1 - \epsilon\sin(\omega t))$. Then after substitution and dropping of ϵ^2 terms:

$$u_t + u_* u_x = -\frac{\lambda u_* u}{Q_0} + \nu u_{xx} ,$$

which gives the equation for the transition function as

$$a'(t) = - \left(iku_* + \frac{\lambda u_*}{Q_0} + k^2\nu \right) a(t) .$$

Thus, once again this gives a result of stability. While this result *is* somewhat physically reasonable, it says that pulsation alone cannot drive meandering. This still

does not account for the observation that the onset of pulsation induces a transient meandering state.

3.7.4 Temporal Meandering Stability- Varying Flux with Constant Amplitude II

To demonstrate that the cause here is most likely non-linear, consider again linearization of the u equation including fluctuations in Q (initially with constant amplitude) such that $Q = Q_0(1 - \epsilon \sin(\omega t))$. However, this time further include the additional non-linearity:

$$u_t + u_* u_x = -\frac{\lambda u_* u}{Q_0 + \epsilon \sin(\omega t)} + \nu u_{xx} .$$

After all, the actual pulsation was lost through the previous linearization (ω). This leads to the equation for the transition function as follows:

$$a'(t) + \left(iku_* + \frac{\lambda u_*}{Q_0} + k^2 \nu \right) a(t) = F(t) ,$$

where

$$F(t) = \frac{-\lambda u_*^2 \epsilon \sin(\omega t)}{Q_0(1 - \epsilon \sin(\omega t))} e^{ikx}$$

Also, let

$$P(t) = iku_* + \frac{\lambda u_*}{Q_0} + k^2 \nu .$$

This equation can still be solved with the use of an integration factor.
Define $\mu = exp(\int P(t)dt)$. Then

$$\frac{d}{dt}(\mu a) = \mu F(t) \Rightarrow a(t) = \frac{1}{\mu} \int \mu F(t)dt .$$

Here $\mu = e^{P(t)t} \Rightarrow$

$$a(t) = e^{-P(t)t} \int \frac{-\lambda u_*^2 \epsilon \sin(\omega t)}{Q_0(1 - \epsilon \sin(\omega t))} e^{P(t)t} e^{ikx} dt .$$

This integral is obviously not an easy task, but making a small time approximation will be enough. Through experiment it is known that pulsation without noise will die out. All that is necessary is to see that for small time there is initial transient behavior. In practice, this means considering t small enough so that $sin(\omega t) \approx \omega t$ and $e^{P(t)t} \approx 1$. Then the above integral expression for the transition function simply becomes

$$a(t) = \frac{-\lambda u_*^2 \epsilon \omega}{Q_0} e^{ikx} \int \frac{t}{(1 - \epsilon \omega t)} dt = \frac{-\lambda u_*^2 \epsilon \omega}{Q_0} e^{ikx} \int \frac{-1}{\epsilon \omega} + \frac{1}{\epsilon \omega (1 - \epsilon \omega t)} dt$$

$$= \frac{-\lambda u_*^2}{Q_0} e^{ikx} \int (-1 + \frac{1}{(1 - \epsilon \omega t)}) dt = \frac{\lambda u_*^2}{Q_0} e^{ikx} (t + \frac{1}{\epsilon \omega} \ln(1 - \epsilon \omega t)) \ .$$

So finally, after a little non-linear stability analysis, it is shown that *initially* the instability grows linearly, but the exponential will quench this linear growth pretty quickly and thus destroy this approximation. Further, in reality, it is known that the contact angle will be playing a very significant role on the dynamics in this stage of the stream development. Therefore, other than a somewhat weak confirmation that this model does agree with experimental observations, *i.e.* that pulsation starts the process, one cannot really take it much further.

Chapter 4

Quantitative Analysis of Experiments and Comparison with Theory

4.1 Spectral Scaling Law

The presented here is based on approximately 200 flow images on various substrates acquired with a high-resolution computer-controlled digital camera. The time intervals between the pictures were random and long enough for the flow patterns to be statistically independent. From each image at time t_m , the deviation of the stream from the centerline $h_m(x)$ was extracted as the function of down-stream distance x. From members of the ensemble $h_m(x)$, $m = 1, ..., 200$, the power spectra $S_m(k)$ was then computed, where wavenumber $k = 2\pi/\lambda$ corresponds to a spatial wavelength λ.

While the power spectra $S_m(k)$, based on single images, are rather noisy, the spectrum produced by averaging over the ensemble $S(k)$ manifests a smooth graph with apparent power-law scaling $S(k) \sim k^{5/2}$ over the span of about two decades (Figure 4.1). Note that averaging over as few as 30 realizations from the ensemble produces a smooth graph with the same power-law exponent. Deviation from this

Chapter 4. Quantitative Analysis of Experiments and Comparison with Theory

scaling is noticeable only for $k \geq k_{max} \simeq 5cm^{-1}$, corresponding to physical scales smaller than the characteristic stream width. The largest physical scale that can be acquired (and thus the smallest wavenumber) is constrained by the 2.4 m streamwise extent of the experimental arrangement.

The scaling behavior is a persistent feature of all the experiments, representing a universal characteristic of the problem of the flow down a partially wetting incline. One important conclusion from the power law behavior is that the leading wavelength associated with meandering instability claimed by previous authors does not exist in the fully developed meandering state. The results were repeated for three surfaces: acrylic (contact angle $57 \pm 2°$) , acrylic with hydrophobic coating (contact angle $74 \pm 5°$) and polypropylene (contact angle $99\pm^{4°}$). The results for spectra and basin area (see below) for these surfaces appear indistinguishable.

To compare the experimental results with the theory, numerical simulation of Equations. 3.7 were performed over a long time ($t \sim O(10,000)$) and computed an average of the spectrum for the deviation of centerline for an ensemble $h_m(x) = h(x, t_m)$ using a sequence of time points t_m. This spectrum is also presented in Figure 4.1. The only fitting parameter is the normalization for noise strength $\eta(x, t)$, taken as a constant for all runs. This theory faithfully reproduces the scaling behavior up to the largest physically relevant values of k corresponding to the droplet forcing width.
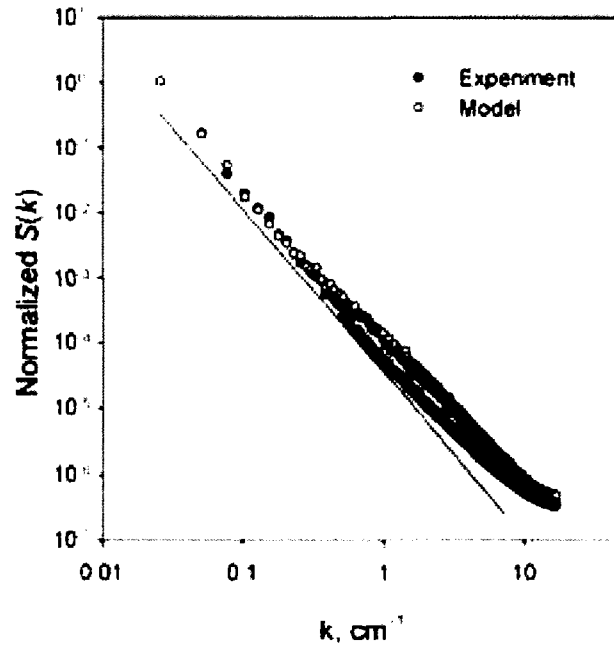
Figure 4.1: Experimental and model comparison of scaling for ensemble average stream profile spectra, all converging to a -5/2power law

Chapter 5

Further Generalizations and Comparison with Rivers

While it is not the attempt of this thesis to provide a model of rivers, some comparison between systems will be addressed. Due to the striking visual similarity, many scientists have contemplated comparison between these two systems. The overwhelming consensus has been that the mobile boundary (erosion) causes meandering instabilities in rivers, and surface tension causes meandering on inclined planes, see ([27], [13], [14], as a few examples). Most previous work on the inclined plane problems makes this assumption and focuses on trying to understand initial stream behavior and predict the leading order wavelength for instabilities due to surface tension, see [20], [14], [1]. For these reasons, there has not been clearly defined quantities to compare between these two systems. Because this thesis considers the fully developed stream profiles, these models are more akin to rivers than previous work and have, therefore, provided potential quantities for comparison. This chapter will develop this framework in the context of stochastic analysis.

5.1   Second Rescaling

The system introduced in Chapter 2 can be further simplified by a temporal rescaling. This is done by postulating that the meanders move slowly with respect to the velocity of the fluid. Letting $h \rightarrow \epsilon h$, the variation equation can be simplified to

$$\frac{dh}{dx} = \frac{v}{u} \ .$$

This allows one to calculate h_{xx} in terms of u and v and eliminate h.

For this first approximation, the lubrication terms proportional to λ will also be neglected. Note that both these approximations are increasingly valid as Q increases, and are clearly valid at the scale of rivers. The final system becomes:

$$\frac{du}{dt} + u\frac{du}{dx} = g\cos(\theta) + \nu u_{xx} + \eta_x \tag{5.1}$$

$$\frac{dv}{dt} + u\frac{dv}{dx} = \nu v_{xx} + (\frac{\gamma}{\rho l})\frac{\partial}{\partial x}(vu) + \eta_y \ . \tag{5.2}$$

5.2   Analytic Analysis of System (5.1, 5.2)

In this section, analysis on the reduced system derived previously is summarized. The exact details of how one solves these problems is outlined more explicitly within the supplemental material found in the Appendix . Because all this work can be found explicitly derived in text books, I omit it from the main body of this thesis. For the purpose of the current work it is enough to know that:

1. The equations derived in Chapter 2 reduce to a rather tractable system.

2. There are solutions to these equations which can be found analytically.

3. These solutions provide useful scaling laws.

4. This approach lays a foundation for a novel method to compare the two systems (erosive versus nonerosive systems) and possibly a way to help model real river systems.

Another important part of the subsequent discussion is the structure of the noise term η. For rivers, one should take $\eta(x,t)$ as white noise with the correlation $< \eta(x,t)\eta(x_0,t_0) >= A\delta(x-x_0, t-t_0)$. The idea used in Chapter 3 (that the noise on the inclined plane is due to droplets) will no longer suffice. More likely, the forces felt by rivers are at all scales due to inhomogeneous underlying topology, not just some average drop size. This stochastic approach to addressing underlying topology has been used before, see [44]. The use of Brownian, or white, noise is actually good. Much work has been done studying integration against Brownian noise and therefore this will lead to an analytical solution (in stochastic sense) for the system (5.1, 5.2). The solution will be shown to yield a 1/6 meandering exponent.

5.2.1   The Downstream Equation

Rewriting the downstream equation

$$\frac{du}{dt} + u\frac{du}{dx} + \nu u_{xx} = \Gamma \tag{5.3}$$

This is simply a random forced Burger's equation where
$\Gamma = \eta_x - g\cos(\theta)$.
With the use of a Cole-Hopf transformation, see ([45] Chapter 3.2) and the Feynman-Kac formula, see ([46] Chapter 8.2) The solution can be written as:

$$u(x,t) = -\lambda\frac{\partial}{\partial x}\left(\frac{1}{\sqrt{4\pi t}}\left(\int e^{\frac{|x_t-y|^2}{4t}}f(y)dy\right)e^{-\frac{\Gamma}{\lambda}\int_0^t x_s ds}\right).$$

5.2.2   The Transverse Equation

Recall the transverse equation 5.2:

$$\frac{dv}{dt} + (u - \frac{\phi}{u})\frac{dv}{dx} - (\frac{\phi u_x}{u^2})v - \nu v_{xx} = \eta_y \tag{5.4}$$

where $\phi = (\frac{\gamma}{\rho l})$.

Note the terms multiplying v and v_x are stochastic since the noise generated in the u equation is now coupled. Here again a Feynman-Kac technique plays a role, while additional complexity is encountered due to the term proportional to $\frac{dv}{dx}$. Nonetheless, the solution to this equation can again be written in terms of the expectation value as

$$v(x,t) = E\left(f(x_t)e^{\int_0^t \alpha(X_s)dB_s - \frac{1}{2}\int_0^t \alpha(X_s)^2 ds - \int_0^t \beta(X_s)ds}\right)$$

where $\alpha = (u - \frac{\phi}{u})$ and $\beta = (\frac{\phi u_x}{u^2})$.

5.3   Second Structure Function and the Scaling Exponent

Start by defining the second-order structure functions $s_f = \int |f(x+l) - f(x)|^2 dx$ as in [47], [33] and assume scaling $s_h \sim l^{2p_h}$, $s_u \sim l^{2p_u}$, and $s_v \sim l^{2p_v}$. Then the powers are related as $p_h = p_v - p_u$.

As was seen previously, by disregarding the lubrication friction terms by setting $\lambda = 0$ and setting η to be white noise then the u equation is simply a noise-driven Burger's equation which can be solved exactly, giving $p_u = 2/3$ (See [45] Section 7.5 with p=0 corresponding to white noise). On the other hand, the v equation can also be solved exactly under these assumptions, yielding $p_v = 3/4$ (Birnir [33] Section 6). From the equation for p_h, one can conclude that $p_h = 1/12$.

Sadly, in the current experimental case, setting any realistic value of $\lambda > 0$ destroys the scaling $p_h = 1/12$. Also, numerics show that the characteristic time for the system to evolve $p_h = 1/12$ scaling for any realistic initial conditions is so large that it can only be observed after several km downstream. It is nevertheless interesting that the meandering exponent $p_h + 1 \simeq 1.16$ agrees (within error bounds) with that of mature rivers (~ 1.1 Maritan [48]).

While these results are somewhat heuristic, for the river system this is quite

48

suggestive. It says the disagreement between the Meandering exponent and the Hack's Law scaling might be understood as follows: The v equation is experiencing classical turbulent scaling due to the noise in this system. However, due to large scale flooding events the u equation is scaling like Burger's shocks. The meandering exponent is a competition between these two effects, *i.e.* $h_x\, u/v = 3/4 - 2/3 = 1/12$, and hence $s_h \sim 1/6$.

The reason this is a heuristic argument rather than a conclusive proof lies in the fact that, implicitly, this argument compares scaling related to time scales. When the kinematic condition is used to say h_x scales like $\frac{v}{u}$, one assumes something that has not been derived rigorously. Namely, for the u equation this assumes a scaling like Burger shocks, see [45], which occur at the time scale of large flooding events. For the v equation, it is assumed the scaling is turbulence, Birnir [33], which is happening at a shorter time scale than the floods.

In reality, this suggests a competition between two behaviors at two time scales is responsible for the observed meandering exponent. In the shorter time scale, the v equation propagates into the transverse direction with a 3/4 scaling, suggestive of the curves attempt to reach the limit of continuity (*i.e. H'older continuous of order 1/4* , Birnir [33]). However, on a longer time scale, floods scaling as Burger shocks with exponent 2/3, keep trying to straighten out the river and hence decreasing the meandering exponent from 3/4 to 3/4-2/3=1/12. This implies the second structure function should scale as 1/6. With the problem now well stated, one should go back and calculate these time scales explicitly to make this argument fully rigorous.

5.4 Hack's Law

As another test of the theory, Figure 4.1 plots the area enclosed between the meandering stream and its centerline as a function of downstream distance. The deviation of the model from the power law is likely due to the length scale associated with the forcing (characteristic droplet size 1-5 mm). The area grows as $x^{7/4} = x^{1.75}$ with
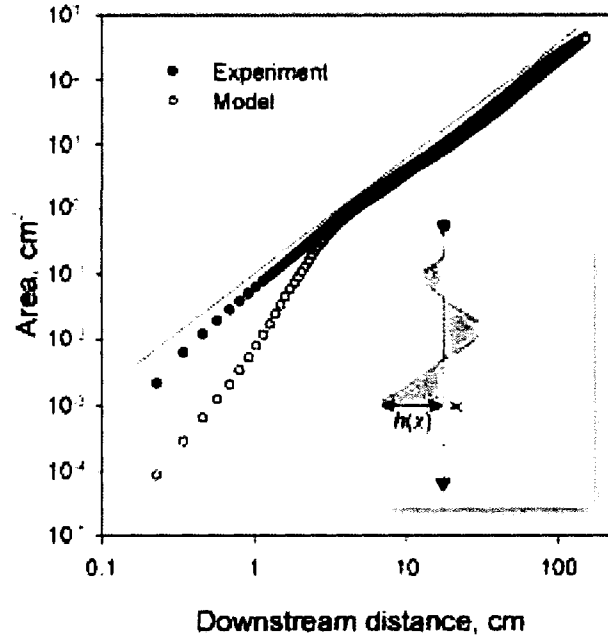
Figure 5.1: Scaling law for model and experiment of area between stream center line and symmetry line versus stream length, both give a 3/4 power law

the distance, consistent with the power law $k^{5/2}$ of the spectrum. Surprisingly, it is the same growth law for the growth of the area of a river basin versus length of the river (discovered by Hack 1957 [16]). In the lab setting, there is clearly no basin per se and no side streams forming that basin. Figure 4.1 deliberately avoids plotting Hacks law data for rivers on the same graph here for fear of misleading readers into thinking that the experiment is describing river basin erosion. This is how it has appeared in publication, see [9] and this result should not be considered in any way questionable.

However, as Figure 5.2 shows, an overlap of the properly scaled data for Hacks law in Figure 4.1 with the river data from Rigon *et al.* (1996) [4] is nearly perfect. The power law is the same but there is an extreme difference in the scales, the data is made to overlap by scaling both area and length by a large factor (red overlay on the plot).

To avoid confusion, note that overlapping our data with those from real rivers is somewhat dangerous due to the variation reported in the exponent in Hacks law
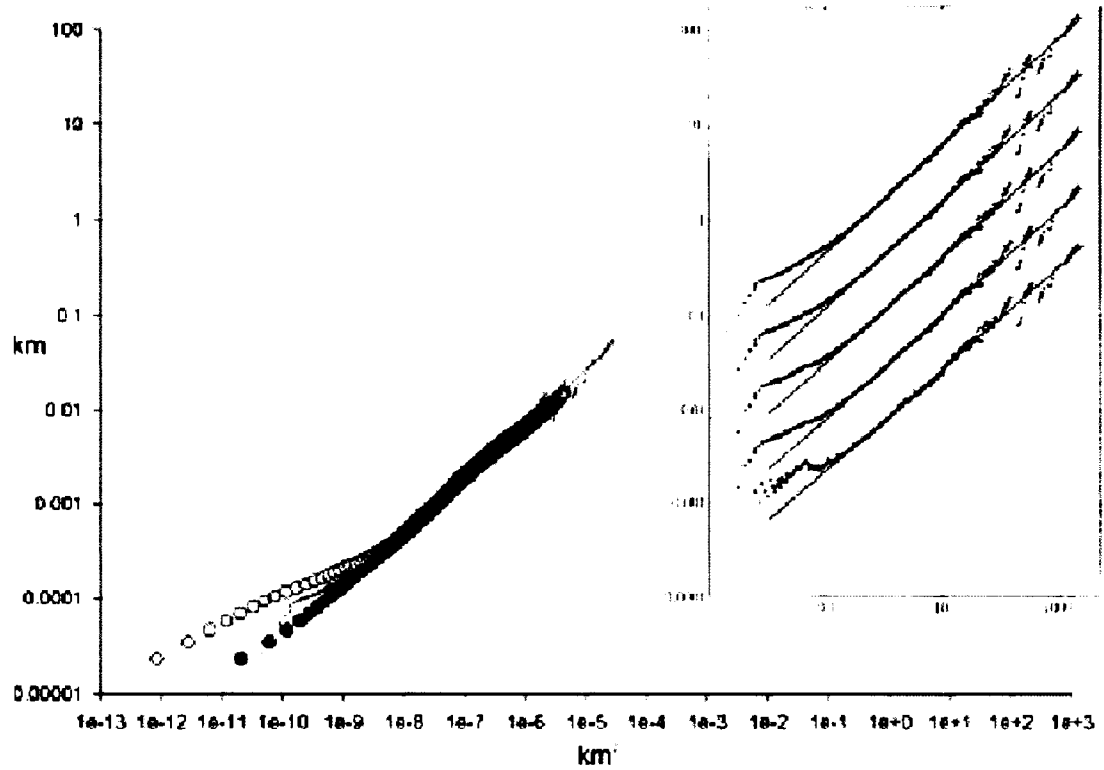
Figure 5.2: Our Data (filled and hollow circles, left) versus data for Hack's Law (On Hack's Law, Rigon *et al.* , [4] right).

depending on the river types, see [35]. Though this is mainly of concern at very large scales where plate techtonics become important. Also, the area spanned by rivulets and area of river basins are very different. Basins fan out from their outlet whereas the rivulets fan out from their source. There are no side streams on lab rivulets, nor are there multiple sources of water (like rain) in lab experiments. The coincidence in the scaling exponents is nevertheless interesting.

Chapter 6

Works in Progress and Future Directions

6.1 Building Back the Dynamics

How does one correctly build the dynamics back into this model? At this point, it has been shown that the spectrum for all measured data was constant for long-time ensemble averages. However, the dynamics can be quite different as a function of surface. Explicitly, as the contact angle decreases, the amplitude of meanders increases while the time scale of meanders decreases.

These are not properties which are captured through previous analysis, nor properties which can currently be predicted with this model. Here is where the dynamic contact angle can no longer be neglected.

When the previous derivation considered surface tension contributions in section 3.3, the curvature in the xy-plane was considered, but that in the yz-plane was neglected, just using the average area $A = lw$. This was clearly a crude approximation for the free surface profile, and indeed it is amazing this model could get as far as it did. Now, consider how one could build this feature back in.

A similar idea (as was used in the xy-plane), based on variational methods, will be

Chapter 6. Works in Progress and Future Directions

used to calculate the free surface profile which minimizes the surface energy. With this one could more accurately predict cross-sectional areas and therefore *at least* implement better averaging strategies.

This similarly to before implies finding a curve which minimizes the functional

$$E = \gamma \int_{-w}^{w} y\sqrt{1 + y_z^2}dy \ .$$

With the use of Lagrange multipliers this means solving the Euler equation

$$\frac{\partial \phi}{\partial y} + \frac{d}{dy}\frac{\partial \phi}{\partial y_z} = 0$$

where

$$\phi(\lambda) = E - \gamma \int_{-w}^{w} \lambda\sqrt{1 + y_z^2}dy \ .$$

The difficulty of this problem is not in solving the Euler equation above, rather it is with the boundary conditions which must satisfy

$$\frac{dy}{dz}(-w) = \theta_a(t) \quad \frac{dy}{dz}(w) = \theta_r(t) \ .$$

Here $\theta_a(t), \theta_r(t)$ represent the advancing and receding contact angles as a function of time. The choice of convention (which labeled advancing/receding) was completely arbitrary. One can now see the difficulty with further advancement. Until there is an established way to predict the complex contact angle dynamics, this analysis cannot continue.

One possibility which has not been investigated carefully is that there may exist a relationship between the two components of curvature (*i.e.* that in xy versus yz planes). If it is possible to simply formulate how much the advancing and receding contact angles change from equilibrium, as a function of the xy curvature, there may still be hope of advancement.

53

6.2 Slow flows

As has been mentioned previously in this paper, for slower flow rates observations are quite different. In particular, Le Grande-Pietera *et al* [5] provide a bifurcation diagram (Shown in Figure 6.1) showing where transitions should exist between stationary meandering and dynamic meandering for flow rate as a function of inclination angle. Because the flows considered in this work are much higher than those, this anomalous pinning behavior was not of significant interest in the beginnings of this work. The fact that they claimed all large enough flows are unstable, however, was quite disturbing. As another plausible explanation of why streams might pin at low
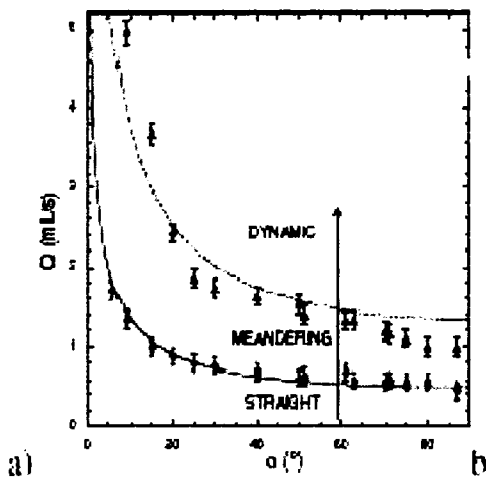
Figure 6.1: Dynamic to Static Meandering Transition from Le Grande-Piteira *et.al.* [5]

flow rates, rather than a balance of a destabilizing surface tension and stabilizing inertia, consider that plastics are highly susceptible to large static charge. With water being a polar molecule this may be important, especially for small flow rates. A series of preliminary tests have been conducted to verify this hypothesis and while the *real* work still remains, these results are worth mentioning now.

First, Dr. Thompson at CSMATE [49] conducted some experiments where he let a small discharge of water run down a uniformly charged plastic surface. He then

waited for several weeks for the surface to be completely dry. Upon measuring the surface charge distribution, he found that it had been permanently deformed by the stream. These results have been reported indirectly elsewhere. After quite extreme efforts to clean their surfaces Schmuki [3] reports:

> ... Additionally, an initially dry surface was found to be essential for reproducible measurements, otherwise the rivulet tended to follow the path that had already been wetted.

Another test of this hypothesis was performed in the Mechanical Engineering Department at the University of New Mexico where the plastic surface was rubbed with a soft cloth to "charge it up" as much as possible. Then, flow rates were inspected much higher than those reported stationary by Le Grande-Pitiera (100ml/min). Amazingly, meandering patterns would pin after some small transient time, and then remain fixed (for up to 24 hours). This further put the influence of charge into the light as a possible additional mechanism required to explain pinning events.

In the previously derived model, the boundary term, found through the lubrication approximation, was inversely proportional to Q. Hence, as this value decreases one would expect this surface interaction to become more dominant and the approximation used less valid.

What is exciting about this possibility is that if the hypothesis is true one should expect to be able to control stream flow through use of surface charges. Modeling this electrostatic coupling, however, is (while not impossible) a very challenging problem, and certainly beyond the scope of this dissertation.

6.3   Slowly eroding surfaces

The reported fact that erosion leads to a meandering instability is a well accepted result among geophysicists, see for example [13]. This belief is so strong that publications reporting similar statistical properties between erosive and non-erosive systems

Chapter 6. Works in Progress and Future Directions
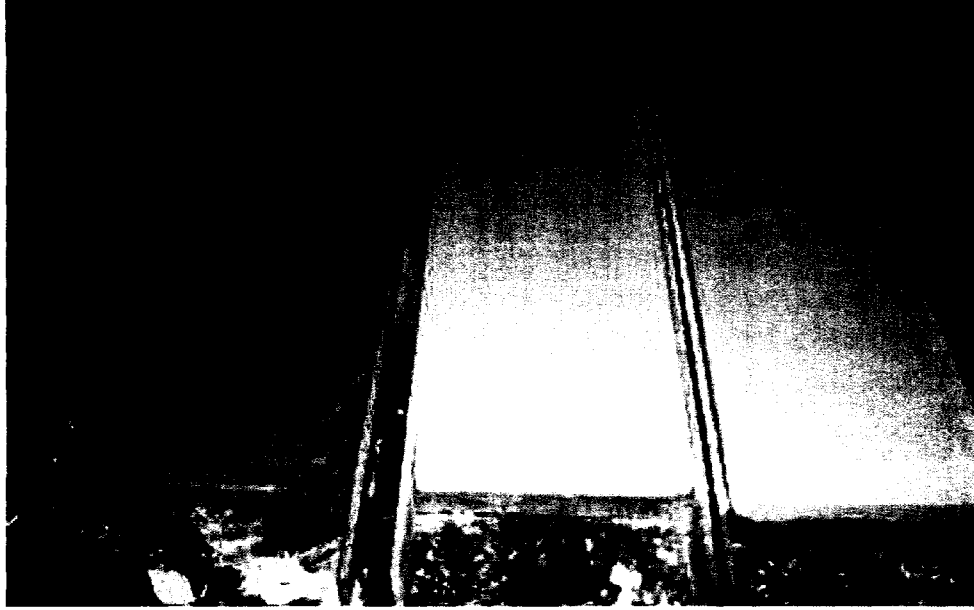
Figure 6.2: New surfaces being used, modeling clay, smooth joint compound, rough joint compound (left to right)

have been severely attacked in the referee stages of peer review. While this point is clearly true for systems where there is substantial erosion per unit time, it is not so obvious for streams where the erosion rate becomes very slow compared to the mass flux of the stream.

Consider the relevant forces. The two most important forces should be the shear experienced by the surface $\sim \nu\rho\frac{\partial u}{\partial z}$, and the force between particles (chemical bonds, electro-static attraction, gravity, etc), which gives a force per unit surface area σ_*. Define a dimensionless number

$$K := \frac{\nu\rho\frac{\partial u}{\partial z}}{\sigma_*} \ .$$

For $K \leq 1$ one would expect no erosion as inter-particle force is larger than the shear trying to tear them apart.

One could then pose the question: will the meandering instability be present in streams for any $K > 1$? For materials like sand and dirt where there is minimal particle cohesion beyond that provided by gravity ($K \gg 1$) from physical observation one knows meandering occurs for large K. It is true, in general σ_* could be somewhat

Chapter 6. Works in Progress and Future Directions

complicated to calculate for many materials. Nonetheless, the question remains, will slowly eroding systems (moderate $K > 1$) meander under parameters which would yield steady states for non-eroding surfaces?

A series of preliminary experiments has been built to address this question. By making 1 inch slabs of various semi-soft solids experiments will observe how the initial channels are formed under constant flow rates. The first series of investigations were done using a common joint compound [50] (limestone, plaster paris, perolite, and a polymer) (Figure 6.2). The results were *somewhat* encouraging. After two weeks of continuous constant flow, small perfectly straight channels had begun to form (approximately 0.5 mm deep). It was, however, also clear that the evolution process was well beyond reasonable timelines. No one wants to run experiments that take months to years per run.

The second series of experiments, currently in progress, use modeling clay as the substrate. It is too early to make well informed comments about the erosion behavior, but the goal of these experiments should be clear. This work will continue into the future, and represents but one of the current directions this work is headed.

SECTION III.

Figure 6.3: Underwater sand ripples in nature

Nature uses only the longest threads to weave her patterns, so that each small piece of her fabric reveals the organization of the entire tapestry.
Richard Feynman

Chapter 7

Underwater Sand Ripples
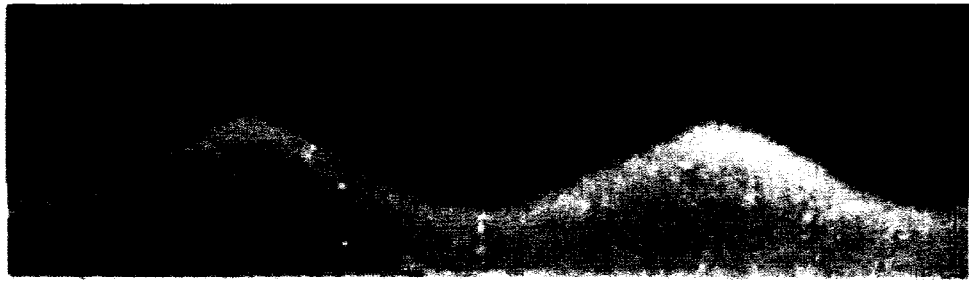
Figure 7.1: Example of Underwater Sand Ripples in the lab [6]

Through the first two sections of this thesis several types of averaging and approximation techniques were used to simplify physics enough to model it from nearly first principles. The next section of this work explores how to approach problems when the underlying physics is simply too difficult to write down from first principles in any reasonable way.

Consider a flat bed of sand subjected to oscillating flow from above. This situation is very natural as it describes most sandy coastlines. One may even be intimately familiar with this from their experience of walking barefoot into the ocean on a sandy beach, and feeling the wave-like structure of the sand beneath their feet.

There are many reasons why people would like to understand the evolution of the bottom of the ocean, especially near coastlines. Yet again, there is a vast amount of

complexity in such a system making it a challenging problem to model.

If one considers the wave-like structure of the sand-water interface in nature, a large range of pattern formation possibilities can be observed, with beautiful transitions between specific patterns, see Figure 6.3. The first work can be traced back to A. Hunt, *On the formation of the ripplemark* (1882) [51], and G. Darwin, *On the formation of the ripple-mark in sand* (1883) [52]. The foundation for studying such systems in a lab setting were pioneered by Ayrton and Bagnold [53], [54] almost 100 years ago. Experimental work on this problem has continued until present day, some examples being [55], [56], [57].

Theory for this problem is however very difficult, and now lags far behind experimental data. The reason for this is that the interface dynamics are governed by the coupled phenomena of turbulent flow from above and non-locally conserved granular transport from below. Each of these two problems alone is quite challenging, let alone coupling the two.

For this reason, the current work begans to develop an amplitude equation based on symmetry arguments and conservation laws, which provides another approach to modeling this system [58].

7.1 Problem Statement

When a bed of sand is exposed to an oscillating flow from above with great enough force to lift sand grains, the bed becomes unstable. As individual grains become mobile, aggregation occurs and "rolling grain ripples" initially develop [54]. Given time to develop, these small rolling grain ripples begin to coarsen into stable "vortex ripples" [11], see Figure 7.2. The exact nature of this evolution process has been noted to be subject to the initial bed preparation. Two schools of thought have developed as to how to consider these structures. One approach is to consider this pattern development as an intrinsic instability of a flat bed to oscillatory flow, leading to a wavy bottom [59]. The second approach is to look at this as the tendency for
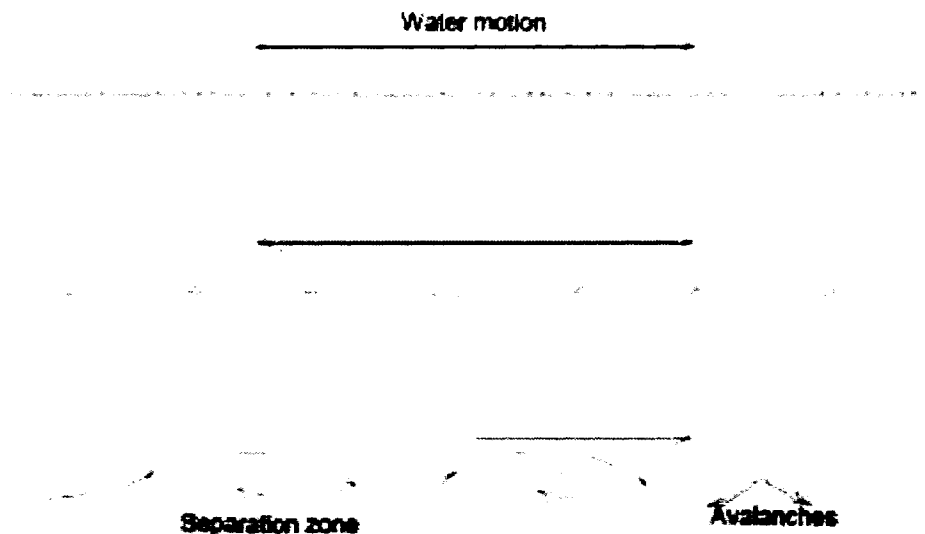
Figure 7.2: Development of Underwater Sand Ripples [6]

loose grains to lump together [60]. Either way, the flat bed is unstable to a certain band of wave vectors which are larger than that set by the initial instability.

It has been shown that the final wavelength selected is set by the amplitude of the external flow with minimal dependency on frequency [61], [62]. Also worth noting is that the frequency can be shown to affect the final shape of a ripple as well as lead to secondary instabilities [57], though these effects are beyond the current considerations.

The final wave length selection is governed by the separation vortex appearing in the trough on the lee side of the ripple crest, whose maximal size is set by the amplitude of the water motion near the bottom. The separation process is also what makes the hydrodynamics of sand ripples so difficult, since the only simple model for such flows (the boundary layer approximation) becomes singular at separation points. Currently no simple model exists which can predict separated flow along an arbitrary height profile short of solving the full Navier-Stokes equations. Work has

been done along this dirrection, for example, Restrepo *et. al.* [63] created a three-dimensional model for the formation of off shore sand structures using non-linear weakly interacting shallow water wave theory.

7.2 Experiments

Though I was not directly involved in the design or data collection for these experiments, I was able to see these experiments run, and had a direct interaction with those running them while in Denmark [62]. For the sake of the reader, I will briefly outline these experiments. There were two independent experiments to study the 1D system, as well as a third experiment for studying the 2D system. Figures of the various schematics, as well as actual apparati, can be found in the Appendix. Thorough experimental accounts can also be found in [62], [64].

In all cases, the idea was similar: to oscillate a tank of water, with a bed of sand on the bottom, using a fixed amplitude and frequency and observe the dynamics of the interface and structure of the steady state. The primary difference between the two 1D experiments was the circular version has true periodic boundary conditions. For the focus of this work, only the 1D model and experiment will be addressed in detail. However, in closing, Section 7.6 will make a few last remarks concerning generalization to the 2D system.

Some of the most important realizations that came through these experiments were:

1. Steady states would develop.

2. The maximal slope of the fully developed ripples is close to the angle of repose for wet sand, $23°$.

3. The final wavelength selected is related to the driving amplitude by the relation $\lambda \approx 1.3a$ and only minimally connected to frequency.

7.3　1D Amplitude Equation

As discussed previously, currently no simple model exists which can predict separated flow along an arbitrary height profile (short of solving the full Navier-Stokes equations). When one adds to this the fact that the flow is turbulent and the complications of the granular dynamics, current understanding is far from a model for the dynamics that would make it possible to derive an amplitude equation from first principles.

Even with such a model, understanding the ripple structures becomes a problem of keeping track of small long-time changes, resulting from differences, almost equal and opposite, occurring in each stroke. The best model currently available, Andersen [65], [66], does this by assigning to the ripples a transport function, which predicts the amount of transport in each half stroke, depending on the ripple size. This model has been successful in predicting certain properties of the ripple patterns, but relies on the representation of a height profile in terms of elementary ripples making the creation of new ripples somewhat artificial.

In the amplitude equation developed here, the periodic forcing will not appear explicitly. The interest is in the long-time behavior in the sense that the model should try to reproduce experimental observation made on time scales that contain many periods. The height function $h(x, t)$ appearing in the amplitude equation is thus equivalent to the height of the drive.

7.3.1　Model Derivation

The construction of this model will rely solely on symmetry considerations and conservation laws. Hence, the equation developed must account for:

1. Conservation: There should be a global conservation of sand.

2. Symmetry: There should he horizontal symmetry of solution across any whole number of oscillation periods.

3. Asymmetry: Ripples in steady state often have noticeable top-bottom asymmetry.

4. Instability: A flat bed should be unstable.

5. Ripple Growth: The flat bed should grow via coarsening to a fixed wavelength based on angle of repose condition.

7.3.2 Building in Angle of Repose Condition

To address each of these requirements, this thesis will build up a PDE for the interface in a series of steps. First, this model must grow or decay based on the slope of the sand compared to that of the angle of repose. Let the angle of repose be defined as ϱ. Hence, consider:

$$h_t = A(h_x^2 - \varrho^2)h_{xx} \ .$$

This starting point provides the necessary condition for growth or decay based on the sand pile slope compared to the angle of repose [67]. Positive points about this equation include:

1. It grows or decays depending on the size of h_x vs ϱ as needed.

2. It has a wave-structure solution (though triangular final states).

This model lacks several requirements also:

1. The solutions are triangles, which are not the desired final shape

2. These solutions coarsen indefinitely, meaning the final steady state is always 1/2 the domain length in the end.

3. Since triangles have sharp points, this implies solutions are singular.

7.3.3 Resolving Singularities

Though the previous model is not perfect, it is a starting point. To remove the absolutely unnecessary singularities introduce a new term proportional to h_{xxxx} (some-
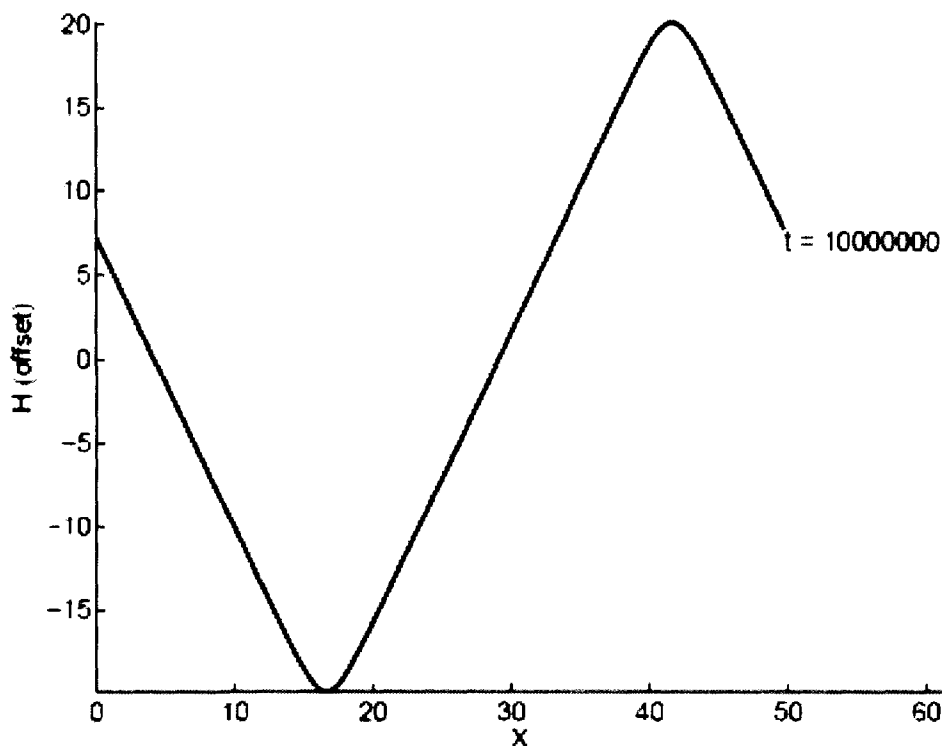
Figure 7.3: A steady state solution for equation (7.5) with $B = 0$

times called hyperviscosity) the equation becomes

$$h_t = A(h_x^2 - \varrho^2)h_{xx} - \nu h_{xxxx} .$$ (7.1)

Here the strength of ν now controls the smoothness of the tips. This is not the first time 7.1 has been written down. Already in 1989 [68] this equation was posed for surface interface evolution in the context of Molecular Beam Epitaxy.

7.3.4 Solving (7.1)

Consider explicitly how the curvature of the tips is controlled by ν. Given the steady state form of this equation:

$$0 = A(h_x^2 - \varrho^2)h_{xx} - \nu h_{xxxx} .$$ (7.2)

65

Re-writing this a little differently and setting $A = 1$, this is equivalent to

$$\frac{\partial}{\partial x}\left(\frac{1}{3}h_x^3 - \frac{\varrho^2}{2}h_x - \nu h_{xxx}\right) = 0 \ .$$

Upon the substitution $w = h_x$ and setting the integration constant equal to zero

$$\nu w_{xx} = \frac{w^3}{3} - \frac{\varrho^2}{2}w \ .$$

Now, setting the right hand side to be minus the derivative of the "potential"

$$\frac{\partial U}{\partial x} = \frac{w^3}{3} - \frac{\varrho^2}{2}w \ ,$$

implies the "potential"

$$U = -\frac{w^4}{12} + \frac{\varrho^2}{4}w^2 \ .$$

Hence, this implies $\frac{\partial}{\partial x}\left(\frac{\nu}{2}w_x^2 + U\right) = \frac{\partial}{\partial x}(K + U) = 0$, a classic result of conservation of energy. Stated slightly differently,

$$w_x = \sqrt{\frac{2(E - U)}{\nu}} \ .$$

The behavior near the tips should be triangle-like and ν should be sen to somehow controls the strength. The "turn around point" for this system (*i.e.* the tips) are where $U = 0$. Near $U = 0$ the potential is dominated by the parabolic term in w. This approximation along with a binomial expansion to first order can be written

$$w_x = \sqrt{\frac{2E}{\nu}}\left(1 + \frac{w^2\varrho^2}{4E}\right) \ .$$

Hence, for $\{-\delta, \delta\}$ a small interval around zero

$$x(w) = \frac{2E}{\nu}\int_{-\Delta}^{\Delta}\frac{1}{1 + \frac{w^2\varrho^2}{4E}}dw \ ,$$

which has the solution

$$x(w) = \frac{2E}{\varrho\nu} \tan^{-1}\left(\frac{2\sqrt{E}w}{\varrho}\right) .$$

This shows that for non-zero ν this is not singular, and further, near the tips the derivative looks like an inverse tangent, hence triangular. Therefore, as suggested previously, this additional term removes singularities and makes the tops of the curves look more like the experiment.

However, there is still a top-bottom symmetry, and these solutions still coarsen indefinitely. The linear Fourier transformation gives the dispersion relation

$$D(k) = \varrho^2 k^2 - \nu k^4 .$$

It is easy to see this gives a maximum value at $k_{max} = \sqrt{\frac{\varrho^2}{2\nu}}$. This being the most unstable mode, implies initially this will be the wavelength first arrived at. From this point, ripples are then squeezed out one by one in a coarsening process as discussed in Politi [69] at a rate $\sim \ln(t)$. The method for finding coarsening laws is to study the phase diffusion equation. A general procedure, along with examples, can be found in Politi [70].

7.3.5   Top-Bottom Asymmetry

To address the top-bottom asymmetry, consider the following contribution to 7.2 the previous equation so it has the form

$$h_t = A(h_x^2 - \varrho^2)h_{xx} - \nu h_{xxxx} + B(h_x^2)_{xx} . \tag{7.3}$$

The strength of the term B now controls the top-bottom asymmetry. While a rigorous mathematical justification is neglected as to why this is, simulation shows it is true, see Figure 7.4. This type of term has been looked at previously in the context of conserved KPZ equation Putkaradze [71]. Now, the only problem with this equation
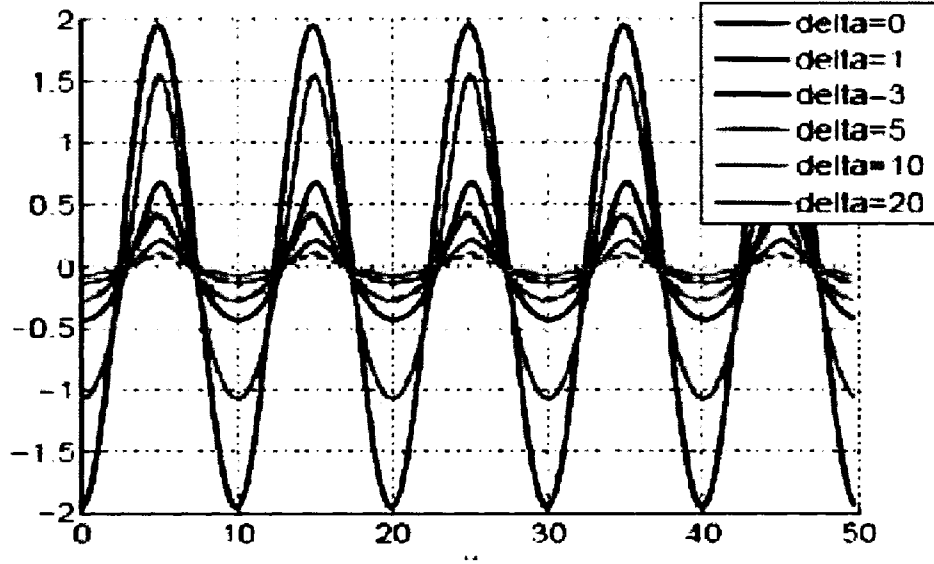
Figure 7.4: Steady state solutions to (7.5) for various delta[6]

is that the coarsening still continues indefinitely!

Models incorporating different combinations of these terms have been looked at, see [69], [71], [72], [73]. The study of coarsening processes themselves have gained recent attention because this idea shows up in many unrelated systems. In fact, this behavior is not uncommon for any system with a local conservation law Politi [69], [70].

It is not clear however that there should be a local conservation law at work. Sand is picked up and carried by the flow. Globally, the sand does not leave the container, but locally, the sand is not conserved.

Considering this system in terms of the linear dispersion relation (which is the same as the previous section since only a nonlinear term has been added), it is clear this solution should grow indefinitely because all these small k-values are still positive (unstable).

7.3.6 Resolving Indefinite Coarsening

Having unstable modes smaller than a sand grain, or larger than the domain itself, are clearly non-physical situations. This constraint sets a reasonable maximum band of unstable modes available to this system. Implementing this idea means adding an additional "Swift-Hohenberg type" [74] linear term to the equation:

$$h_t = A(h_x^2 - \varrho^2)h_x x - \nu h_{xxxx} + B(h_x^2)_{xx} - ah \ . \tag{7.4}$$

The addition of such a term means there is no longer local conservation, but as was discussed previously, that is not necessarily incorrect.

Again, consider what this does to the linear dispersion relation

$$D(k) = \varrho^2 k^2 - \nu k^4 - \epsilon \ .$$

Because the smallest k values are now negative (stable), it finally stops coarsening at a fixed wavelength. At this point, the equation has almost all the desired properties.

This system *should* have global conservation of sand. To fix the last issue, simply subtract the average value of h from the linear term so that

$$h_t = A(h_x^2 - \varrho^2)h_{xx} - \nu h_{xxxx} + B(h_x^2)_{xx} - a(h - \bar{h}) \tag{7.5}$$

(7.5) is the equation now considered as a model for 1D sand ripple dynamics.

7.3.7 Proof of Global Conservation

A local conservation law would imply that

$$\frac{\partial h}{\partial t} = \frac{\partial J}{\partial x}$$

69

where J is the mass flow, or in this case the surface current. In other words:

$$\int_{x_1}^{x_2} \frac{\partial h}{\partial t} dx = \int_{x_1}^{x_2} \frac{\partial J}{\partial x} dx \Rightarrow$$

$$\frac{\partial}{\partial t} \int_{x_1}^{x_2} h dx = J(x_2) - J(x_1)$$

i.e. the way mass is changing within the region (x_1, x_2) is dictated by the difference of what is flowing in at x_1 vs out at x_2. In the case that $\epsilon = 0$, (7.5) can be written explicitly with

$$J = -\left(\frac{1}{3}(h_x)^3 - \varrho^2 h_x\right) - \nu h_{xxx} - \delta(h_x^2)_x$$

and the local conservation law holds. However, as has been seen previously, the model requires a non-zero ϵ to stop indefinite coarsening. Further, in this problem there is not local conservation as was discussed above. However, to ensure global conservation implies:

$$\int_0^L \frac{\partial h}{\partial t} dx = \int_0^L -\epsilon(h - \bar{h}) + \frac{\partial J}{\partial x} dx \Rightarrow$$

$$\frac{d}{dt} \int_0^L h dx = -\epsilon \int_0^L (h - \bar{h}) dx + J|_0^L \Rightarrow$$

$$L \frac{\partial \bar{h}}{\partial t} = -\epsilon(L\bar{h} - L\bar{h}) = 0$$

which is satisfied, since there is no mass flux outside the domain *i.e.* $J|_0^L = 0$.

7.4 Numerical Results

After the models development, a new student, Teis Schnipper, began working on this system. In particular, he performed extensive numerical investigations of (7.5). For more details concerning this work see [64]. The goals were to do an exhaustive investigation across parameter space, to look at final wavelength selection, and consider dynamic transitions between different steady states of model compared to experiment.
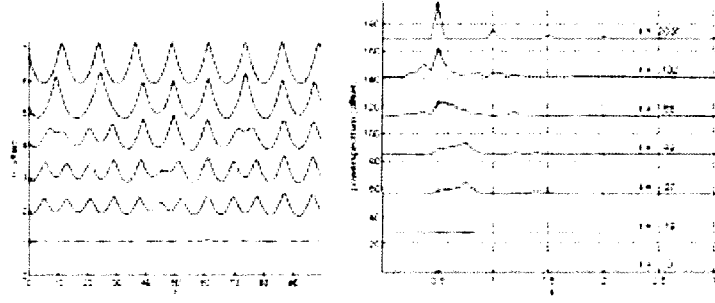
Figure 7.5: Left: Time evolution of an initially flat bed to ripples (bottom to top); Right: Spectral evolution of this same process. [6]

For any study across parameter space, it is always best to reduce the system as much as possible with non-dimensionalization. In this case, non-dimensionalizing this system leads to

$$h_t = (h_x^2 - 1)h_{xx} + h_{xxxx} + \delta(h_x^2)_{xx} - \epsilon(h - \bar{h}) \tag{7.6}$$

where $\epsilon = a\nu A^{-2}\varrho^{-4}$ and $\delta = B\nu^{-\frac{1}{2}}A^{-\frac{1}{2}}$, corresponding to the time-scale $T = \frac{\nu}{A^2\varrho^4}$ and length-scale $X = \frac{1}{\varrho}(\frac{\nu}{A})^{\frac{1}{2}}$. Figure 7.5 shows snapshops of the numeric evolution
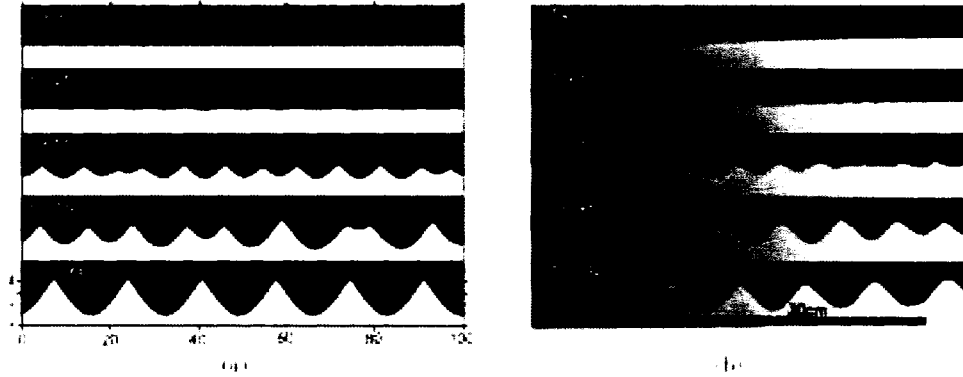
Figure 7.6: Left: Numerical simulation; Right: Experimental evolution [6]

of an initially flat bed perturbed by 10% random fluctuations. As one can see, this profile does grow to a steady state with the required profile properties.

As another test of the dynamics, Figure 7.6 shows the side by side comparison

71

of the numeric and experimental dynamic evolution of the interface profile. As one can see, qualitatively the behavior is quite similar.
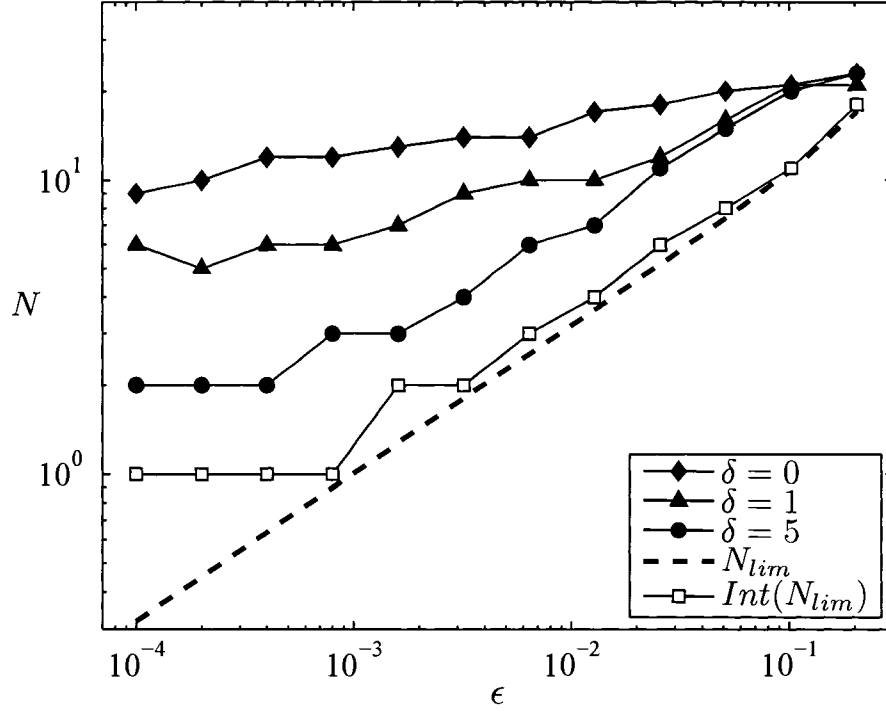
Figure 7.7: Numerical Scaling of the steady state wavelength (N) as a function of ϵ and δ [6]

Another interesting, but unexpected result, given by this equation is the scaling law for the steady state wavelength as a function of the dimensionless parameters ϵ and δ, see Figure 7.7. Understanding this point analytically is actually quite nontrivial and will be further addressed in Chapter 8.

7.5   Modeling Bifurcations

Simulations were also run to inspect the profile, $h(x,t)$, evolution when the wavelength chosen as the initial condition was different from the preferred choice of steady state. It is easy to enter this type of initial condition into a numeric solver and watch it evolve back to the correct steady solution. These dynamics have also been studied carefully in experiment, and therefore they offer another immediate place for comparison.
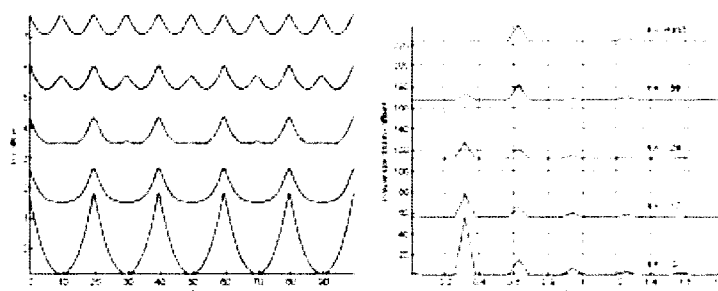
Figure 7.8: Left: Numeric simulation of evolution in time, Right: Experimental evolution of sand ripple in time [6]

As one can see from Figure 7.8, the doubling transition can be modeled. However, in many cases the model has a large decay of amplitude associated with this transition [64] which is not seen in true experiments. The models' ability to take ripples out easier than it puts them back in is not understood. It may be a consequence of the model itself, or perhaps it is a finite domain length effect? Nonetheless, it shows an obvious limitation with need of further consideration.

7.6   2D Models, Experiments, and Future Work

As was stated previously, in the context of this problem, experiments and data run far ahead of theory. While there is no fully developed 1D model, extensive experiments have been done that look at 1D, 2D and 2D-skew driven ripple formation processes. Obviously, the 2D systems are far more realistic for modeling nature. However, they

are also far more complicated. Additional schematics, experimental pictures and a few remarks about the 2D system can be found in the Appendix. These experiments were the primary focus of [62].

While the 1D amplitude equation does provide a nice first approach to the problem, generalization into 2D is not obvious. In the case of the 2D experiments (which were the focus of [62]), many secondary types of instabilities have been reported, see Figure (7.9). Notice, in the 2D system instabilities are found as a function of *both* frequency and amplitude. While beautiful to observe, these additional complexities pose their own challenges to modeling.

[6]
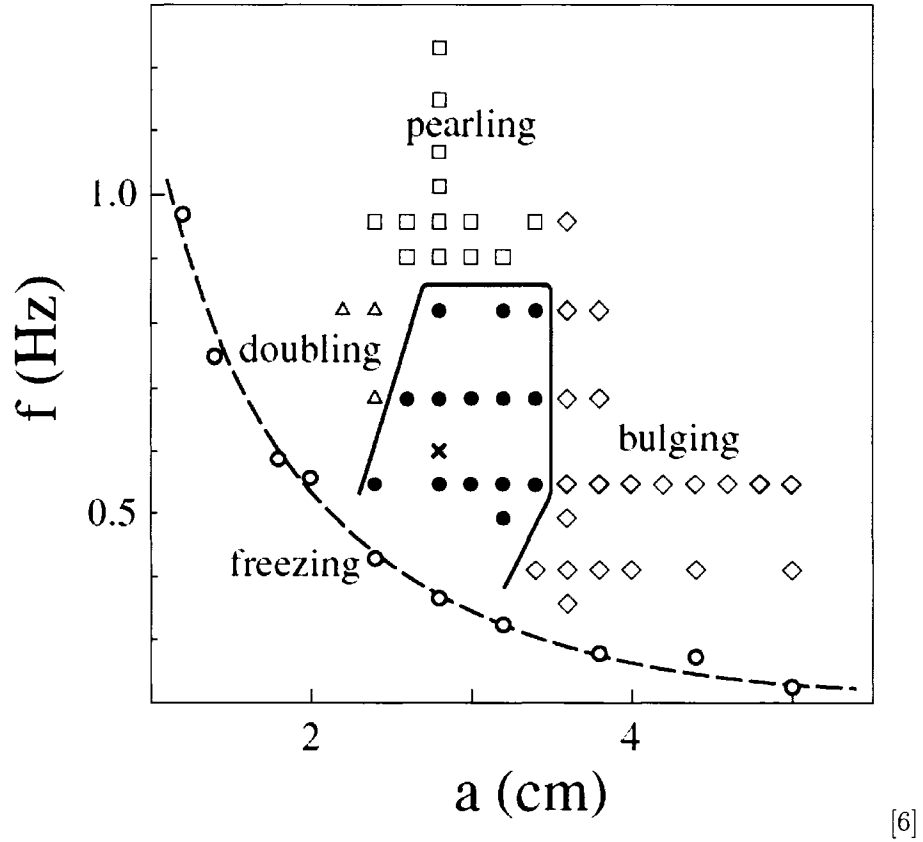
Figure 7.9: Experimental Stability Diagram in 2D, frequency vs amplitude

Consider the simple addition of a passive term into the second dimension such

that 7.6 becomes:

$$h_t = (h_x^2 - 1)h_{xx} + h_{xxxx} + \delta(h_x^2)_{xx} - \epsilon(h - \bar{h}) + h_{yy} \ .$$

Unfortunately, this equation cannot provide the rich complexity of secondary instabilities observed in the real physical system. One should actually not be surprised that the addition of a passive term in y is not enough. The true coupling must be taken into account much more carefully. Figure 7.10 shows a snapshot in time of a 2D simulation in response to a "forcing frequency" different from the initial condition (a fixed wavelength skew to the x-axis, while the "drive" is along the x-axis). This image demonstrates the only type of instability into the second dimension possible for the given system as it changes shape.
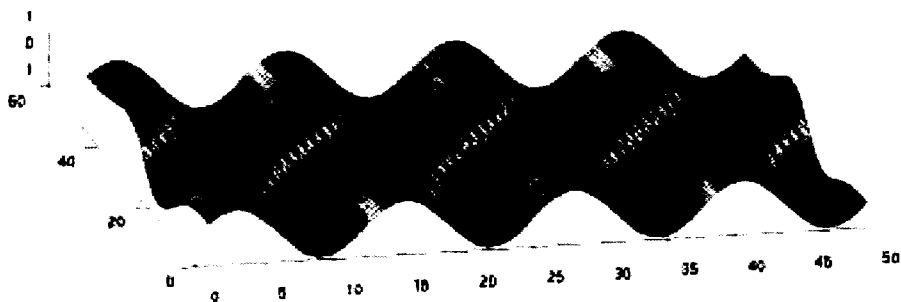
Figure 7.10: Snapshop of numerical two dimensional ripple evolution under skew drive

Chapter 8

Lie Prolongation and Wavelength Selection

The wavelength selection process in non-linear systems can be quite complicated. Therefore, Figure 7.7 presents an interesting challenge to try and understand analytically. Clearly, in the asymptotic limit as $\delta \gg 1$ the steady state wavelength converges to k_*, but as δ decreases there is significant difference in the scaling law for ϵ versus the final wavelength.

In this problem, as has been seen, linear stability analysis fails to predict the correct final wavelength. Further, the non-linear integrals required to transform the full equation prove exceedingly tough. Therefore, a new approach is necessary.

A general approach to studying symmetries of differential equations has been developed, see Olver [75]. Through this process one derives explicitly the infinitesimal generators for the group action which transforms solutions to solutions. A novel idea for the application of this algorithm is now presented in an attempt to understand Figure 7.7. The advantage to this approach is the ease with which it can be expanded to include parameters, as well as its ability to deal with non-linear terms without any approximations or loss of terms.

8.1   Selection and Interrupted Coarsening

As was mentioned previously, an interesting, but not expected, additional complex behavior of this equation is found in the selected wavelength for a given (ϵ, δ). For linear theory this problem is clearly determined, simply find the maximum value of k (*i.e.* k_{max}) for the unstable band. For many nonlinear systems, one will see that eventually the smallest positive value of k (*i.e.* k_*) becomes the steady state. When all values of $k \geq 0$ are positive, the system will find k_{max} first, and then coarsen in time squeezing out one ripple at a time until the final state is one-half period of the domain length.

In such systems, one can in many instances predict the scaling of how these ripples will come together in time Politi [69], [70]. In some instances of nonlinear systems, such as this one, the final selected wavelength is neither k_* nor k_{max}. Rather, it starts out like a coarsening process and then stops at some intermediate value $k_* < k < k_{max}$. This process is known as interrupted coarsening. Figure 7.7 shows that the final wavelength, as a function of ϵ, for various values of δ changes the scaling dramatically. For the limit $\delta \gg 1$ it does converge to k_{max}. However, for moderate values of δ, it does not.

Interupted coarsening is not uncommon in many other amplitude equations. Because there is immediate access to this numeric data, this model provides an interesting "toy model" to probe for an understanding of this phenomena.

8.2   Lie Prolongation Algorithm

The details of this algorithm, along with examples, are presented in Olver [75], and details of this calculation for the ripple evolution equation can be found in the Appendix. Here the outline will be layed for how this algorithm works in general and the novel idea for applying it to non-linear wavelength selection.

Chapter 8. Lie Prolongation and Wavelength Selection

Given a scalar PDE of the form

$$u_t = f(x, t, u, u_x, u_{xx}, ..) \,,$$

one would like to calculate the group actions $G_\epsilon : (u_1 \rightarrow u_2)$ where u_1, u_2 are symmetry solutions of the given PDE. One must, of course, assume solutions exist. Let the above PDE be defined as Δ. To do this calculation one then postulates that the infinitesimal generator of this transformation, an element of the Lie algebra, should have the form:

$$\bar{v} = a_1(x, t, u)\partial_x + a_2(x, t, u)\partial_t + \phi(x, t, u)\partial_u \,.$$

Now, with the use of Lie's prolongation method, one calculates the n-th order prolongation of $\bar{v}$ where n corresponds to the highest degree derivative in the PDE. For example:

$$pr^{(1)}\bar{v} = \bar{v} + \phi^x \partial_{u_x} + \phi^t \partial_{u_t} \,.$$

The n-th order prolongation is then applied to the system Δ to arrive at the symmetry equation in terms of the unknown coefficients. Using total derivatives (again see Olver [75]) one expands these coefficients and impose the condition provided by Δ (*i.e.* equate $u_t = f$ everywhere u_t appears). This yields a system of ODEs to solve by matching the coefficients, called the determining system. Once solved, it provides the infinitesimal generator of the symmetries.

Integrating against the one parameter group (provided by the exponential map) one transforms the infinitesimal generator (*i.e.* the element of the Lie algebra) to the group action (*i.e.* similarity transformation) itself. In principle this approach will always work to find symmetries (provided they exist), though in practice it can become quite challenging to get through this procedure.

8.3   Application to 1D Amplitude Equation

In the 1D amplitude equation, the interest is in the final wavelength as a function of ϵ and δ. Hence, the novel idea here is to expand this system with ϵ and δ considered as independent continuous variables in addition to x and t. Therefore, ultimately one looks for the group action $G : h_1(x, t, \epsilon, \delta) \rightarrow h_2(x, t, \epsilon, \delta)$ where h_1 and h_2 are two solutions to (7.6) as a function of ϵ and δ.

This implies looking for a generator of the form:

$$\bar{v} = a_1(x, t, \epsilon, \delta)\partial_x + a_2(x, t, \epsilon, \delta)\partial_t + a_3(x, t, \epsilon, \delta)\partial_\epsilon + a_4(x, t, \epsilon, \delta)\partial_\delta + \phi(x, t, \epsilon, \delta)\partial_h$$

where a_i, $i = 1, 2, 3, 4$ and ϕ are the unknown coefficients left to find.
Upon applying the fourth order prolongation of $\bar{v}$ onto (7.6) (*i.e.* $pr^{(4)}\bar{v}[\Delta]$) one arrives at the symmetry equation

$$
\begin{aligned}
\phi^t =\ & 2\phi^x h_x h_{xx}^2 + \phi^{xx}(h_x^2 - 1) - \epsilon\phi - a_3 h + \phi^{xxxx} + 2a_4 h_{xx}^2 + \\
& 4\delta\phi^{xx} h_{xx} h_{xxx} + 2a_4 h_x h_{xxx} + 2\delta\phi^x h_{xxx} + 2\delta\phi^{xxx} h_x \ .
\end{aligned}
\tag{8.1}
$$

The details of calculating ϕ^x- ϕ^{xxxx}, substituting them into above, and equating the coefficients are left as calculations for the Appendix.

While the solution to this system is beyond the scope of this manuscript, the outline is now layed for how this calculation can be done. The hope is that after solving this system one should be able to determine the similarity transformations given by the group action. This would allow for a understanding of how a steady state solution h scales as a function of the parameters ϵ and δ. The only remaining obstacle from here is actually solving this system.

Because there is a relation between h_{max} (height of ripple top) and λ (wavelength), set by the angle of repose, once these solution scalings are known one can deduce the scaling analytically which are presented numerically in Figure 7.7

Chapter 8. Lie Prolongation and Wavelength Selection

This is a somewhat tedious calculation in general. Nonetheless, the potential to use this algorithm in such a setting could provide very useful in a similar way for many other problems. Further, if this type of calculation proved useful, the algorithm for deriving these determining systems could be automated fairly easily.

8.4 Conclusion

In conclusion, this work presents many new and interesting methods for addressing the complexity of fluid-solid interactions and interfacial dynamics. In the context of two physical systems, it has been shown averaging techniques, stochastic methods, variational calculus, amplitude equations, and prolongations can be useful tools in modeling and analyzing these systems.

Through the first two Sections of this work, models were developed to explain the steady states, as well as some of the statistical properties of the dynamic flows. Experimentally, the existence of steady states was proven. The mechanism of meandering was found to be perturbations in flow rate. Analysis of fully developed stream profiles showed the existence of a universal power-law scaling for the spectrum of long-time ensemble averaged stream profiles. This power-law was confirmed both experimentally and numerically. Consideration of the scaling between the length of stream and the area between its symmetry line and stream center line gave a 3/4 power law, similar to that found for rivers by Hack [16]. Further, using rescaling arguments this model was able to reduce to a system which shares many of the same features of river systems, including the scaling of the second structure function for stream curvature. This result suggests a possible explanation for the observed data about real world rivers and a connection between erosive and non-erosive meandering systems.

This work has opened the door to many future directions of study also. One should go on to consider the limits with respect to both surface contact angle and flow rates. The dynamic contact angle should be incorporated into the model to understand temporal dynamics of meandering. Further, more studies should be conducted to investigate the connections between erosive and non-erosive surfaces.

In the third Section of this work, focus shifted to another type of problem where modeling from first principles becomes impossible. In this context an amplitude equation was derived from conservation and symmetry considerations. It was shown that such modeling can produce reasonable results. In deriving this model, the

question of nonlinear wavelength selection became important. In closing this thesis, a novel approach to studying such behavior was presented.

Throughout the third Section, again many open questions have been posed. Generalizations into the second dimension should now be considered. Further, the calculation set up in Chapter 8 for the determining system for the 1D amplitude equation must be solved. If this calculation is shown to work, it has great potential to work similarly in many other circumstances.

In closing, the ideas presented within this work give a solid foundation for many years of future study, as well as nice advancements to a pair of complicated 100+ year old problems.

References

[1] K. Mizumura and M. Yamasaka. Analysis of meandering water rivulets of finite amplitude. *Journal of Hydraulic Engineering*, 123:995–1003, 1997.

[2] Photo provided by the Southern Florida Water Management District.

[3] P. Schmuki and M. Laso. On the stability of rivulet flow. *J. Fluid Mech.*, 215:125–143, 1990.

[4] R. Rigon, I. Rodriguez-Iturbe, A. Maritan, A. Giacometti, D. G. Tarboton, and A. Rinaldo. On Hack's law. *Water Resources Research*, 32:3367–3374, 1996.

[5] N. Le Grand-Piteira, A. Daerr, and L. Limat. Meandering rivulets on a plane: A simple balance between inertia and capillarity. *Phys. Rev. Lett*, 96:254503, 2006.

[6] Many thanks to Teis Schnipper and Frederik Bundgaard for providing me numerical and experimental pictures, many of which come from their thesis' and a few from a joint publication.

[7] K. Mertens, V. Putkaradze, and P. Vorobieff. Braiding patterns on an inclined plane. *Nature*, 430:165, 2004.

[8] K. Mertens, V. Putkaradze, and P. Vorobieff. Morphology of a stream flowing down an inclined plane. Part 1. Braiding. *J. Fluid Mech.*, 531:49–58, 2005.

[9] B. Birnir, K. Mertens, V. Putkaradze, and P. Vorobieff. Morphology of a stream flowing down an inclined plane. Part 2: Meandering. *J. Fluid Mech.*, (under consideration), 2008.

[10] B. Birnir, K. Mertens, V. Putkaradze, and P. Vorobieff. Noise driven meandering streams. *Physical Review Letters*, (under consideration), 2008.

[11] C. Ellegaard T. Schnipper, K. Mertens and T. Bohr. Amplitude equation and long range interactions in under water sand ripples in one dimension. *Phys. Rev. Lett.*, under consideration.

References

[12] J. Gratton C. Perazzo. NavierStokes solutions for parallel flow in rivulets on an inclined plane. *J. Fluid Mech.*, 507:367–379, 2004.

[13] G. Parker. On the cause and characteristic scales of meandering and braiding in rivers. *J. Fluid Mech.*, 76:457–480, 1976.

[14] K. Mizumura. Meandering water rivulet. *Journal of Hydraulic Engineering*, 119:1205–1222, 1993.

[15] P.G. deGennes. Wetting: statics and dynamics. *Rev. Mod. Phys.*, 57:827–863, 1985.

[16] J. Hack. Studies of longitudinal stream profiles in Virginia and Maryland. *U.S. Geological Survey Professional Paper*, 294-B, 1957.

[17] J. Thomson. On the windings of rivers in alluvial plains. *Royal Soc. London Proc.*, 25, 1876.

[18] A. Einstein. *Naturwissenschaften*, 14:223–224, 1926.

[19] G. Seminara. Meanders. *J. Fluid Mech.*, 554:271–297, 2006.

[20] S.H. Davis. Moving contact lines and rivulet instabilities. 1. The static rivulet. *J. Fluid Mech.*, 98:225–242, 1980.

[21] R.H. Weiland and S.H. Davis. Moving contact lines and rivulet instabilities. 2. Long waves on flat rivulets. *J. Fluid Mech*, 107:261–280, 1981.

[22] G.W. Young and S.H. Davis. Rivulet instabilities. *J. Fluid Mech*, 176:1–30, 1987.

[23] J.B. Culkin and S.H. Davis. Meandering of water rivulets. *AIChE J.*, 30:263–267, 1984.

[24] T. Nakagawa and J.C. Scott. Stream meanders on a smooth hydrophobic surface. *J. Fluid Mech.*, 149:89–99, 1984.

[25] T.M.S. Nakagawa. Rivulet meanders on a smooth hydrophobic surface. *Int. J. Multiphase Flow*, 18:455–463, 1992.

[26] H.-Y. Kim, J-H. Kim, and B.H. Kang. Meandering instability of a rivulet. *J. Fluid Mech.*, 498:245–256, 2004.

[27] M. Gorycki. Hydraulic drag: a meandering initiating mechanism. *Bull. Geol. Soc. Am.*, 84, 1973.

[28] E. Andrews. G. Parker. On the time development of meandering bends. *J. Fluid Mech.*, 162:139–156, 1985.

References

[29] S. Ikeda, G. Parker, and K. Sawai. Bend theory of river meanders. 1. Linear development. *J. Fluid Mech.*, 112:363–377, 1981.

[30] T.M.S. Nakagawa and R. Nakagawa Jr. A novel oscillation phenomenon of the water rivulet on a smooth hydrophobic surface. *Acta Mechanica*, 115:27–37, 1996.

[31] Putkaradze V Bohr, T and S Watanabe. Averaging theory for the structure of hydraulic jumps and separation in laminar free surface flows. *Phys. Rev. Lett*, 79:1038–1041, 1997.

[32] K. Mertens. Investigations into the behavior of thin-film flows on an incline. Master's thesis, The University of New Mexico, Albuquerque, 2005.

[33] B. Birnir. Turbulent rivers. *Quarterly of Applied Math*, to appear, 2008.

[34] B. Birnir, J. Hernandez, and T.R. Smith. The stochastic theory of fluvial land-surfaces. *J. Nonlinear Sci.*, 17:13–57, 2007.

[35] P.S. Dodds and D. Rothman. Geometry of river networks. I. Scaling, fluctuations, and deviations. *Phys. Rev E*, 63:016115, 2000.

[36] P.S. Dodds and D. Rothman. Geometry of river networks. II. Distributions of component size and number. *Phys. Rev E*, 63:016116, 2000.

[37] P.S. Dodds and D. Rothman. Geometry of river networks. III. Characterization of component connectivity. *Phys. Rev E*, 63:016117, 2000.

[38] P.S. Dodds and D. Rothman. Scaling, universality and geomorphology. *Annu. Rev. Earth Planet. Sci*, 28:571–610, 2000.

[39] P.S. Dodds and D. Rothman. Unified view of scaling laws for river networks. *Phys. Rev E*, 59:4865–4877, 1999.

[40] Civil Engineering Database: http://cedb.ascc.org/.

[41] C. Clanet. Clepsydrae from Galileo to Torricelli. *Phys. Fluids*, 12:2743–2751, 2000.

[42] Gnu image manipulation program (gimp): http://www.gimp.org/.

[43] Imagetools ©: http://ddsdx.uthscsa.edu/dig/itdesc.html.

[44] T. B. Liverpool and S. F. Edwards. Dynamics of meandering rivers. *Phys. Rev. Lett.*, 75:3016–3019, 1995.

[45] W. Woyczynski. *Burgers-KPZ Turbulence*. Springer, Berlin, Germany, 1998.

[46] B. Oksendal. *Stochastic Differential Equations*. Springer, Berlin, Geremany, 1985.

References

[47] U. Frisch. *Turbulence*. Cambridge University Press, Cambridge, UK, 1995.

[48] Rinaldo A. Rigon R. Giacometti A. Maritan, A. and I. Rodriguez-Iturbe. Scaling laws for river networks. *Phys. Rev. E*, 53:15101515, 1996.

[49] Center for Science Mathematics and Technology Education (CSMATE), Colorado State University.

[50] United States Gympsum Company. ingredients: plaster of paris; limestone; expanded perolite; attapulgite; vinal alchohol polymer.

[51] A. Hunt. On the formation of the ripplemark. *Proc. Roy. Soc. of London*, 34:1–18, 1882.

[52] H. Ayrton. On the formation of the ripple-mark in sand. *Proc. Roy. Soc. of London*, A36:18–43, 1883.

[53] H. Ayrton. The origin and growth of ripple-mark. *Proc. R. Soc.*, 84:285, 1910.

[54] R. A. Bagnold. Motion of waves in shallow water. interaction between waves and sand bottoms. *Proc. R. Soc.*, 187:1, 1946.

[55] A. Stegner and J. E. Wesfried. Dynamical models for sand ripples beneath surface waves. *Phys. Rev. E*, 60:R3487, 1999.

[56] A. Stegner G. Rousseaux and E. Wesfried. Wavelength selection of rolling-grain ripples in the laboratory. *Phys. Rev. E*, 69:031307, 2004.

[57] A. Haaning C. Ellegaard K. H. Andersen T. Bohr J. L. Hansen, M. v. Hecke and T. Sams. Instabilities in sand ripples. *Nature*, 410:324, 2001.

[58] Research internship N.B.I./D.T.U, August 2003-January 2004.

[59] P. Blondeaux. Sand ripples under sea waves part 1. ripple formation. *J. Fluid Mech*, 218:1, 1990.

[60] K. H. Andersen. Wavelength selection of rolling-grain ripples in the laboratory. *Phys. Fluids*, 13:58, 2001.

[61] J. Fredse and R. Deigaard. Mechanics of coastal sediment transport. *World Scientic*, 1992.

[62] F. Bundgaard. *Pattern Formation of Underwater Sand Ripples with a Skewed Drive*. PhD thesis, Niels Bohr Institute, Copenhagen, Denmark, 2003.

[63] J. Restrepo and J. Bona. Three-dimensional model for the formation of longshore sand structures on the continental shelf. *Nonlinearity*, 8:781–820, 1995.

[64] T. Schnipper. Development of an amplitude equation for describing underwater sand ripples. Master's thesis, Technical University of Denmark, Lyngby, Denmark, 2007.

References

[65] M.-L. Chabanol K. H. Andersen and M. v. Hecke. Dynamical models for sand ripples beneath surface waves. *Phys. Rev. E*, 63:066308, 2001.

[66] J. Krug L. R. Sndergaard K. H. Andersen, M. Abel and J. Udesen. Pattern dynamics of vortex ripples in sand: Nonlinear modeling and experimental validation. *Phys. Rev. Lett.*, 88:234302, 2002.

[67] Before my internship in Denmark, Tomas Bohr and Vincent Hakim had originally sat down and postulated this starting point.

[68] Guo H Sun T and Grant M. Dynamics of driven interfaces with a conservation law. *Phys. Rev. A*, 40:6763, 1989.

[69] P. Politi. Kink dynamics in one-dimensional growing surfaces. *Phys. Rev. E*, 58:281, 1998.

[70] P. Politi. When does coarsening occur in the dynamics of one-dimensional fronts? *Phys. Rev. E*, 73:03613, 2006.

[71] T. Bohr V. Putkaradze and J. Krug. Global estimates and shocks for the noiseless conserved KPZ equation. *Nonlinearity*, 10:823, 1997.

[72] J. Krug. Coarsening of sand ripples in mass transfer models. *Adv. Complex System*, 4:353, 2001.

[73] F. Rioual Z. Csahk, C. Misbah and A. Valance. Dynamics of aeolian sand ripples. *Euro Phys. J. E*, 3:71–86, 2000.

[74] M. Cross and P. C. Hohenberg. Pattern formation outside of equilibrium. *Rev. Mod. Phys.*, 65:852, 1993.

[75] P. Olver. *Applications of Lie Groups to Differential Equations*. Springer, New York, NY, 1991.

[76] D. Hilbert R. Courant. *Methods of Mathematical Physics, vol. 1*. Interscience Publishers, Inc, Berlin, Germany, 1937.

[77] L. Perko. *Dynamical Systems*. Springer, New York, NY, 2001.

[78] H. McKean. Turbulence without pressure: Existence of the invariant measure. *Methods and Applications of Analysis*, 9:463468, 2002.

SECTION IV.

Beware of the man who won't be bothered with details. William Feather

Appendix A

Outline of the Braids Model

While it is not the intention of this thesis to reproduce every detail of the analysis preformed on the braids model, the reader should be able to understand these underlying idea's without having to depart from this text. Some of these ideas are relied on heavily in the later derivations of meandering streams. For more explicit details see [7], [8], [32].

$$\frac{d\mathbf{U}}{dt} + \mathbf{U}\nabla\mathbf{U} = \frac{1}{\rho}\nabla\mathbf{P} + g\sin(\alpha)\hat{e}_x + \nu\nabla^2\mathbf{U}$$

To begin a model, start with the boundary layer approximation (BLA) parallel to the plane along with the incompressibility condition $\nabla \cdot \mathbf{u} = 0$. To begin reduction on this system, make the following assumptions:

1. Stationary states have zero time derivatives, *i.e.* $\frac{\partial}{\partial t} = 0$

2. In steady state these exists a symmetry condition, *i.e.* $p(x,y) = p(-x,y)$

3. Transverse dependency of x-velocity is negligible, *i.e.* $U(x,y) \approx U(x)$

4. Downward flux conserved, *i.e.* $U(x)A(x) = Q = constant$

5. Contact angle is constant, *i.e.* $\frac{dp}{dy}(\pm w) = \mp\tan(\theta)$

Appendix A. Outline of the Braids Model

Along with these five assumptions, also consider that to fairly good accuracy the free surface profile at any cross-section in x can be described by a fourth order polynomial of the form

$$p(x,y) = (w^2 - y^2)(a - by^2) .$$

At this point the parameters a and b can be found using conditions 1-5 above.

$$a = \frac{\tan(\theta)}{2w} + bw^2 \tag{A.1}$$

$$b = \frac{15}{8w^5} \left(\frac{Q}{U_x} - \frac{\tan(\theta)w^2}{3} \right) \tag{A.2}$$

Additionally, with the use of this polynomial free surface approximation, one can calculate the average force due to surface tension at each cross-section. In this situation, the surface tension contributions are far larger than those of hydrostatic pressure, hence this will allow calculation of the pressure term in 3.1. One finds that:

$$F(u,w) = \int_{dS} \gamma p(x,y)''' p(x,y) dS \tag{A.3}$$

$$= 3b\gamma \tan(\theta)w^3 + 4b^2\gamma w^6 . \tag{A.4}$$

Substituting this information into (3.1), in component form the system becomes:

$$U_x \frac{\partial U_x}{\partial x} = g\sin(\alpha) - \nu \frac{\partial^2 U_x}{\partial z^2} \tag{A.5}$$

$$(\rho A)U_x \frac{\partial}{\partial x}U_y = F(w, U_x) - \nu \frac{\partial^2 U_y}{\partial z^2}(\rho A) . \tag{A.6}$$

Now using Lubrication theory one can average over z contributions approximating the second derivatives in A equations and therefore reducing the system to coupled ODEs. Lubrication theory is valid when one length scale is much smaller than the others in a fluid problem. In this case the height of the stream is small compared to length or width, therefore approximate the z component of velocity such that:

90

Appendix A. Outline of the Braids Model

1. No slip is satisfied at substrate boundary

2. Shear stress is zero on free surface boundary

Additionally, enforce the average ($i.e$ $\frac{1}{p}\int_0^p U_x(z)dz = U_x$). With this, A becomes:

$$U_x\frac{dU_x}{dx} = g\sin(\alpha) - 3\nu\frac{U_x}{p_{avg}^2} \tag{A.7}$$

$$(\rho A)U_x\frac{d}{dx}(U_x\frac{dw}{dx}) = F(w, U_x) - \nu\frac{U_x}{p_{avg}^2}\frac{dw}{dx}(\rho A) . \tag{A.8}$$

Now, non-dimensionalizing these equations, one arrives at

$$(u \cdot w')' = F(u, w) - \pi_1 u^2 w^2 w' \tag{A.9}$$

$$u \cdot u' = 1 - \pi_2 u^3 w^2 \tag{A.10}$$

where

$$\Pi_1 = \frac{3Q\rho^2\nu(gsin(\alpha))}{\gamma^2} \tag{A.11}$$

$$\Pi_2 = \frac{3Q^5\rho^7\nu(gsin(\alpha)^4)}{\gamma^7} . \tag{A.12}$$

Further, solution analysis may be done to determine critical points, look at linearization around these points, and determine the associated eigenvalue equation. This information may then be used to assess the solution stability and analyze the bifurcation diagram of the system.

For linearization conducted about the constant downstream velocity and constant stream width, the system has two critical points corresponding to:

$$\frac{\Pi_\text{I}}{\Pi_\text{II}u} = \frac{w^2\tan\theta}{3} \tag{A.13}$$

91

Appendix A. Outline of the Braids Model

$$\frac{\Pi_{\mathrm{I}}}{\Pi_{\mathrm{II}} u} = -\frac{w^2 \tan\theta}{15} \ .$$ (A.14)

It can be shown however that equation (A.14) leads to instability. Thus, from (A.13) with Π_2, for the stable critical point one has

$$\begin{cases} u_c = \sqrt{\frac{\tan(\theta)}{3\Pi_2}} \\ w_c = \sqrt{\frac{\tan(\theta)}{\Pi_2 u_c^3}} \ . \end{cases}$$ (A.15)

Consider linearization near the stable critical

$$\begin{cases} u_* = u_c + u_1 \exp(\lambda y) \\ w_* = w_c + w_1 \exp(\lambda y) \end{cases}$$

where u_1 and w_1 are small.

Now, to determine the eigenvalues define

$$F_* = \frac{1}{16}\left[15\frac{\Pi_{\mathrm{I}}}{\Pi_2}\frac{1}{u_* w_*^2} - 5\tan\theta\right]\left[15\frac{\Pi_{\mathrm{I}}}{\Pi_2}\frac{1}{u_* w_*^2} + \tan\theta\right] \ .$$ (A.16)

$$G_* = 1 - \Pi_2 u_*^3 w_*^2$$ (A.17)

where F_* is the non-dimensionalized surface tension force in terms of F_*, G_*, and their derivatives. The eigenvalue problem can be formulated as

$$\det \begin{bmatrix} (u_c\lambda^2 - \frac{\partial F_*}{\partial w_*} + 4\Pi_{\mathrm{I}} u_c^2 w_c^2 \lambda) & -\frac{\partial F_*}{\partial u_*} \\ \\ -\frac{\partial G_*}{\partial w_*} & u_c\lambda - \frac{\partial G_*}{\partial u_*} \end{bmatrix} = 0 \ .$$ (A.18)

To find the eigenvalues implies solving a cubic equation in λ.

$$u_c^2\lambda^3 + (4\Pi_{\mathrm{I}} u_c^3 w_c^2 - u_c\frac{dG_*}{du_*})\lambda^2 - (u_c\frac{d\mathbf{F}}{dw_*} + 4\Pi_{\mathrm{I}} u_c^2 w_c^2)\frac{dG_*}{du_*})\lambda + \frac{d\mathbf{F}}{dw_*}\frac{dG_*}{du_*} - \frac{d\mathbf{F}}{du_*}\frac{dG_*}{dw_*} = 0 \ .$$ (A.19)

The real part of all λ is negative for all parameter values. A pair of complex conjugate

Appendix A. Outline of the Braids Model

eigenvalues corresponds to a solution with oscillating width, *i.e.* braiding. After equation (A.19) is solved numerically, the braid length can be determined as $2\pi/\text{I}'\text{m}\lambda$. When the braid length goes to infinity, *i.e.*, $\text{I}'\text{m}\lambda \to 0$, the stream approaches the rivulet solution.

Appendix B

Variational Methods

In this section the variational derivative is derived which is used in Sections 3.3 and 6.1. Here the thesis strays from the standard notation. Let $\langle \cdot \rangle$ denote the inner product here. Given a functional of the form: $F[\rho(r)] = \int f(r, \rho(r), \nabla\rho(r)) \, dr$, with ρ vanishing at the boundaries of r the functional derivative can be written

$$\langle \delta F[\rho], \phi \rangle \quad = \frac{d}{d\varepsilon} \int f(r, \rho + \varepsilon\phi, \nabla\rho + \varepsilon\nabla\phi) \, dr \Big|_{\varepsilon=0} \tag{B.1}$$

$$= \int \left(\frac{\partial f}{\partial \rho} \phi + \frac{\partial f}{\partial \nabla\rho} \cdot \nabla\phi \right) dr \tag{B.2}$$

$$= \int \left[\frac{\partial f}{\partial \rho} \phi + \nabla \cdot \left(\frac{\partial f}{\partial \nabla\rho} \phi \right) - \left(\nabla \cdot \frac{\partial f}{\partial \nabla\rho} \right) \phi \right] dr \tag{B.3}$$

$$= \int \left[\frac{\partial f}{\partial \rho} \phi - \left(\nabla \cdot \frac{\partial f}{\partial \nabla\rho} \right) \phi \right] dr \tag{B.4}$$

$$= \left\langle \frac{\partial f}{\partial \rho} - \nabla \cdot \frac{\partial f}{\partial \nabla\rho}, \phi \right\rangle, \tag{B.5}$$

where $\phi \in C^1$ is an arbitrary function such that, in the third line explicitly, $\phi = 0$ is assumed at the integration boundaries. Thus,

$$\frac{\delta F}{\delta \rho} = \frac{\partial f}{\partial \rho} - \nabla \cdot \frac{\partial f}{\partial \nabla\rho} \, .$$

This is for the particular case when the functional depends on the function $\rho(r)$ and its first derivative $\frac{d\rho(r)}{dx}$. Gradient notation was used because the generalization

Appendix B. Variational Methods

to $\mathbf{r} = (r_1, r_2, r_3)$ follows immediately. For a more detailed review with higher order contributions and mulit-variable vector functions a fundamental reference is Methods of Mathematical Physics, [76].

Appendix C

Spatial and Temporal Instabilities

In this section, the thesis makes a digression to define some notation and the basic approach taken for performing stability analysis. Spatial stability analysis is straight forward. These systems are ODEs and so it is enough to find the eigenvalues and look at real and imaginary parts, as is the standard technique in any dynamical systems book (for example Perko [77]).

To consider temporal stability is also quite standard. However, notation, and word choices, can make it appear different from book to book. For current purposes the following conventions will be used and demonstrated via example:

Consider the forward/backward Helmholtz equation :

$$u_t = u_{xx} \pm u .$$

This problem can be posed as $u_t = \mathbf{P}u$ where $\mathbf{P} = D^2 \pm 1$ is defined as *the symbol of P*. Further, to consider solutions of the form $u(x,t) = a(t)e^{ikx}$ implies solving an ODE for the *transition function for $a(t)$*:

$$a'(t) = \hat{P}a(t) .$$

Appendix C. Spatial and Temporal Instabilities

In this example, $\hat{P}(ik) = -k^2 \pm 1$. If one assumes $a(0) = 1$, this implies

$$a(t) = e^{\hat{P}t} \Rightarrow u(x,t) = e^{\hat{P}t}e^{ikx} \ .$$

Temporal stability is found by investigation of $e^{\hat{P}t}$, namely if $\Re(\hat{P}(ik)) \leq 0 \ \forall k$, which corresponds indirectly to finite energy. Hence for these simple Helmholtz examples, one can see depending on the sign, they give $e^{(-k^2 \pm 1)t}$, so the plus choice is unbounded or unstable.

Appendix D

Stochastic PDEs

In this section, the basic solution techniques and relevant references which go with Section 5.2 are outlined. The starting point of this section will be the stochastic heat equation under Brownian motion:

$$u_t = \sigma u_{xx} + \frac{d\eta}{dt}$$

$$u(x,0) = f(x) \ .$$

The equivalent Ito's representation of this equation as a stochastic PDE is,

$$du = \sigma u_{xx} dt + d\eta$$

$$u(x,0) = f(x) \ .$$

It is well-known, see for example Oksendal [46], that the solution for $\eta = 0$ can be written in the form

$$u(t,x) = E[f(B_t)]$$

where the E denotes the expectation in the probability space $(\Omega, \mathcal{F}, \mathcal{P})$ where Ω is a set of probabilities, $\mathcal{F}$ a sigma algebra of sets in Ω and P the law of Brownian motion B_t. Here the initial condition $f(x)$ is evolved with the classical heat kernel.

This obviously leaves questions of existence and uniqueness. For detailed proofs on these subjects, (see Oksendal [46] Chapter 9).

If the operator A is the generator of an Ito process X_t, then similarly

$$u(t, x) = E[f(X_t)]$$

solves the initial value problem

$$u_t \quad = \quad Au \tag{D.1}$$

$$u(0, x) \quad = \quad f(x) . \tag{D.2}$$

Now, consider the following generalization of this problem

$$u_t \quad = \quad Au - qu \tag{D.3}$$

$$u(0, x) \quad = \quad f(x) \tag{D.4}$$

where A is a linear operator on u, q is lower bounded, and again the problem is stochastic implicitly. In this case, the problem can be solved by using the Feynman-Kac formula, which can be understood as a generalization of the integration factor. An outline of the proof is as follows. Let $Y_t = f(X_t)$, $Z_t = e^{-\int_0^t q(X_s)ds}$ Then

$$dZ_t \quad = \quad -Z_t q(X_t)dt \tag{D.5}$$

$$d(Y_t Z_t) \quad = \quad Y_t dZ_t + Z_t dY_t = -q(X_t)Y_t Z_t + Z_t dY_t \tag{D.6}$$

or

$$du = Au - qu$$

where $u = Y_t Z_t$ because $dE[Y_t] = E[AY_t]$. Hence, with $u = E[Y_t Z_t]$ this gives the

Appendix D. Stochastic PDEs

Feynman-Kac formula:

$$u(t, x) = E[e^{-\int_0^t q(X_s)ds} f(X_t)] \ .$$

This proof is copied from Oksendal [46] Chapter 8. With this as a foundation, now consider the downstream equation derived in section 5.2

$$\frac{du}{dt} + u\frac{du}{dx} - \nu u_{xx} = \Gamma \ . \tag{D.7}$$

What is nice here is that this equation is actually just the equation solved previously in disguise.

Consider the Cole-Hopf transformation

$$u = -\lambda\frac{\partial}{\partial x}ln(w) = -\lambda\frac{w_x}{w} \tag{D.8}$$

where $\nu = \frac{\lambda}{2}$. Then

$$u_t = -\lambda(\frac{-1}{w^2}w_x w_t + \frac{1}{w}w_{xt}) \tag{D.9}$$

$$u_x = -\lambda(\frac{-1}{w^2}w_x^2 + \frac{1}{w}w_{xx}) \tag{D.10}$$

$$u_{xx} = -\lambda(\frac{2}{w^3}w_x^3 - \frac{3}{w^2}w_x w_{xx} + \frac{1}{w}w_{xxx}) \ . \tag{D.11}$$

Substituting (D.9)-(D.11) into (D.7) results in

$$(\frac{\lambda}{w^2}w_x w_t - \frac{\lambda}{w}w_{xt}) + (\frac{-\lambda^2}{2w^2}w_x w_{xx} + \frac{\lambda^2}{2w}w_{xxx}) = \Gamma \ .$$

With a little rearrangement

$$\frac{\lambda}{w^2}w_x(w_t - \frac{\lambda}{2}w_{xx}) - \frac{\lambda}{w}\frac{\partial}{\partial x}(w_t - \frac{\lambda}{2}w_{xx}) = \Gamma \ .$$

Thus, if u satisfies (D.7) then w satisfies

$$\frac{\partial w}{\partial t} - \frac{\lambda}{2}\frac{\partial^2 w}{\partial x^2} = -\frac{\Gamma x w}{\lambda} \; . \tag{D.12}$$

This is the Feynman-Kac equation which is stochastic since Γ has noise. With this, one can then write the solution as

$$w(x,t) = E(f(x_t)e^{-\frac{\Gamma}{\lambda}\int_0^t x_s ds}) \; .$$

Now combining this with (D.8)

$$u(x,t) = -\lambda\frac{\partial}{\partial x}(\frac{1}{\sqrt{4\pi t}}(\int e^{\frac{|x_t - y|^2}{4t}} f(y)dy)e^{-\frac{\Gamma}{\lambda}\int_0^t x_s ds}) \; .$$

Again, for a rigorous proof see Woyczynski [45] Chapter 3. With this solution for the downstream equation now outlined consider the cross-stream equation. It will be necessary to generalize the previous ideas further to solve this equation. To solve the transverse equation uses the method of Cameron-Martin [78]. Consider

$$\frac{dv}{dt} + (u - \frac{\phi}{u})\frac{dv}{dx} - (\frac{\phi u_x}{u^2})v - \nu v_{xx} = 0 \tag{D.13}$$

where $\phi = (\frac{\gamma}{\rho l})$. Note the terms multiplying v and v_x are stochastic since the noise generated in the u equation is now coupled multiplicatively in v. The transverse equation can be written as

$$\frac{dv}{dt} + \alpha\frac{dv}{dx} - \beta v - \nu\frac{d^2 v}{dx^2} = 0$$

where $\alpha = (u - \frac{\phi}{u})$ and $\beta = (\frac{\phi u_x}{u^2})$. Ito's formulation of this equation as a stochastic PDE is

$$du = \left(-\alpha\frac{dv}{dx} + \beta v + \nu\frac{d^2 v}{dx^2}\right) dt \; .$$

As has been shown previously, the term involving β is just a Feynman-Kac type term which can be accounted for with the generalized integration factor. This mean that

Appendix D. Stochastic PDEs

the solution can be written as

$$v(x,t) = E[f(X_t)]$$

where X_t is the Ito process defined by the equation

$$dX_t = \alpha(X_t)dt + \sqrt{\nu}dB_t \ .$$

By Cameron-Martin the solution can then be written as

$$v(x,t) = E(f(B_t)e^{\int_0^t \alpha(B_s)dB_s - \frac{1}{2}\int_0^t \alpha(B_s)^2 ds}) \ .$$

Combining contributions of terms of the form of Cameron-Martin and Feynman-Kac gives:

$$v(x,t) = E(f(x_t)e^{\int_0^t \alpha(x_s)dx_s - \frac{1}{2}\int_0^t \alpha(x_s)^2 ds - \int_0^t \beta(x_s)ds})$$

where $x_t = B_t$ is Brownian motion. For a rigorous analysis of this equation, including uniqueness results and derivation of the invariant measure, see Birnir [33].

Appendix E

Details of Prolongation Calculation

The details of the prolongation algorithm are rather straight forward though incredibly tedious. The essence lies in expanding out $\phi^x - \phi^{xxxx}$ and substituting them back into the symmetry equation (8.1). To do this involves taking derivatives and chain rules repeatedly. In reality, at this level of computation one should write a symbolic program to save time and energy. However, the necessary time and motivation hinge on showing it is worth doing $i.e.$that it can succeed in answering some otherwise difficult question such as that posed in by Figure (7.7).

For simplicity,consider transformations of steady state solutions only, after all this enough for the question posed by Figure 7.7. The equation becomes

$$(u_x^2 - 1)u_{xx} - u_{xxxx} - \epsilon u + \delta(u_x^2)_{xx} = 0 \ . \tag{E.1}$$

Hence upon applying the fourth prolongation onto (E.1), as was done in Chapter 8 but now without the time-derivative, one arrives at

$$\begin{aligned} 0 = \ & 2\phi^x h_x h_{xx}^2 + \phi^{xx}(h_x^2 - 1) - \epsilon\phi - a_3 h + \phi^{xxxx} + 2a_4 h_{xx}^2 + \\ & 4\delta\phi^{xx}h_{xx}h_{xxx} + 2a_4 h_x h_{xxx} + 2\delta\phi^x h_{xxx} + 2\delta\phi^{xxx}h_x \ . \end{aligned} \tag{E.2}$$

In this calculation, there are three independent variables and one dependent variable.

Appendix E. Details of Prolongation Calculation

This implies the coefficients in equation (E.2) are

$$\phi^x = \phi_x - \phi_u u_x - u_x(a_{1x} + a_{1u}u_x) - u_\epsilon(a_{3x} + a_{3u}u_x) - u_\delta(a_{4x} + a_{4u}u_x) \quad \text{(E.3)}$$

$$
\begin{aligned}
\phi^{xx} = {} & \phi_{xx} + u_x(2\phi_{xu} - a_{1xx} - a_{3ux} - a_{4ux}) + \\
& u_x^2(\phi_{uu} - 2a_{1ux} - a_{3uu} - a_{4uu}) + u_{xx}(-2a_{1x} - a_{3u}a_{4u}) \\
& u_x u_{xx}(-3a_{1u}) - u_x^3 a_{1uu} - u_\epsilon a_{3xx} - u_{x\epsilon}(2a_{3x}) - u_\epsilon u_x(2a_{3ux}) \\
& -2u_{x\delta}a_{4x} - u_\delta a_{4xx} - u_x u_\delta a_{4ux} - u_{x\epsilon}u_x a_{3u} - u_{x\delta}u_x a_{4u} \quad \text{(E.4)}
\end{aligned}
$$

$$
\begin{aligned}
\phi^{xxx} = {} & \phi_{xxx} + u_x(3\phi_{xxu} - a_{1xxx} - a_{3uxx} - a_{4uxx}) + \\
& u_{xx}(2\phi_{ux} - 3a_{1xx} - 2a_{3ux} - 2a_{4ux}) + u_x^2(3\phi_{uux} - 3a_{1uxx} - 2a_{3uux} - 2a_{4uux}) + \\
& u_x u_{xx}(2\phi_{uu} - 9a_{1ux} - 3a_{3uu} - 3a_{4uu}) + u_x^3((\phi_{uuu} - 3a_{1uux} - a_{3uuu} - a_{4uuu})) + \\
& u_{xxx}(-3a_{1x} - a_{3u} - a_{4u}) + u_{xx}^2(-3a_{1u}) + u_x u_{xxx}(-4a_{1u}) + u_x^2 u_{xx}(-6a_{1uu}) + \\
& u_x^4(-a_{1uuu})u_{\epsilon x}(-3a_{3xx}) + u_\epsilon(-a_{3xxx}) + u_x u_\epsilon(-2a_{3xxu}) + u_{xx\epsilon}(-3a_{3x}) + \\
& u_x u_{x\epsilon}(-4a_{3xu}) + u_{xx}u_\epsilon(-3a_{3xu}) + u_x^2 u_\epsilon(-a_{3xuu}) + u_{xx\delta}(-3a_{4x}) + u_{x\delta}(-3a_{4xx}) + \\
& u_{x\delta}u_x(-4a_{4xu}) + u_\delta(a_{4xxx}) + u_\delta u_x(-2a_{4xxu}) + u_{xx}u_\delta(-a_{4xu}) + u_x^2 u_\delta(-a_{4xuu}) + \\
& u_{xx}u_{x\epsilon}(a_{3u}) + u_x u_{xx\epsilon}(-2a_{3u}) + u_x^2 u_{x\epsilon}(-a_{3uu}) + u_x^2 u_{x\delta}(-a_{4uu}) + \\
& u_{xx}u_{x\delta}(-a_{4u}) + u_x u_{xx\delta}(-2a_{4u}) \quad \text{(E.5)}
\end{aligned}
$$

$\phi^{xxxx} =$

$\phi_{xxxx} + u_x(4\phi_{xxxu} - a_{1xxxx} - a_{3xxxu} - a_{4xxxu}) +$

$u_{xx}(5\phi_{xxu} - 4a_{1xxx} - 3a_{3xxu} - 3a_{4xxu}) + u_x^2(6\phi_{xxuu} - 4a_{1xxxu} - 3a_{3xxuu} - 3a_{4xxuu}) +$

$u_{xxx}(2\phi_{xu} - 6a_{1xx} - 3a_{3xu} - 3a_{4xu})) + u_{xx}u_x(10\phi_{xuu} - 18a_{1xxu} - 9a_{3xuu} - 9a_{4xuu}) +$

$u_x^3(4\phi_{xuu} - 6a_{1xxuu} - 3a_{3xuuu} - 3a_{4xuuu}) + u_{xx}^2(2\phi_{uu} - 12a_{1xu} - 3a_{3uu} - 3a_{4uu}) +$

$u_xu_{xxx}(2\phi_{uu} - 16a_{1xu} - 4a_{3uu} - 4a_{4uu}) + u_x^2u_{xx}(5\phi_{uuu} - 24a_{1xuu} - 6a_{3uuu} - 6a_{4uuu}) +$

$u_x^4(\phi_{uuuu} - 4a_{1xuuu} - a_{3uuu} - a_{4uuu}) + u_{xxxx}(-4a_{1x} - a_{3u} - a_{4u}) + u_{xx}u_{xxx}(-10a_{1u}) +$

$+u_{xx}^2u_x(-15a_{1uu}) + u_xu_{xxxx}(-5a_{1u}) + u_x^2u_{xxx}(-10a_{1uu}) + u_x^3u_{xx}(-10a_{1uu}) +$

$u_x^5(-a_{1uuuu}) + u_{\epsilon xx}(-6a_{3xx}) + u_{\epsilon x}(-4a_{3xxx}) + u_{\epsilon x}u_x(-9a_{3xxu}) + u_\epsilon(-a_{3xxxx}) +$

$u_\epsilon u_x(-3a_{3xxxu}) + u_{xx}u_\epsilon(-3a_{3xxu}) + u_x^2(-3a_{3xxuu}) + u_{xxx\epsilon}(-4a_{3x}) + u_{xx\epsilon}u_x(-9a_{3xu}) +$

$u_{x\epsilon}u_{xx}(-5a_{3xu}) + u_{x\epsilon}u_x^2(-6a_{3xuu}) + u_{xxx}u_\epsilon(-a_{3xu}) + u_xu_{xx}u_\epsilon(-3a_{3xuu}) +$

$u_x^3u_\epsilon(-a_{3xuuu}) + u_{xxx\delta}(-4a_{4x}) + u_{xx\delta}(-6a_{4xx}) + u_{xx\delta}u_x(-9a_{4ux}) + u_{x\delta}(-4a_{4xxx}) +$

$u_{x\delta}u_x(-9a_{4xxu}) + u_{x\delta}u_{xx}(-6a_{4xu}) + u_{x\delta}u_x^2(-6a_{4xuu}) + u_\delta(-a_{4xxxx}) + u_\delta u_x(-3a_{4uxxx}) +$

$+u_\delta u_{xx}(-3a_{4xxu}) + u_\delta u_x^2(-3a_{4xxuu}) + u_{xxx}u_\delta(-a_{4xu}) + u_xu_{xx}u_\delta(-3a_{4xuu}) +$

$u_x^3u_\delta(-a_{4xuuu}) + u_{xxx}u_{x\epsilon}(-a_{3u}) + u_{xx}u_{xx\epsilon}(-3a_{3u}) + u_{xx}u_{x\epsilon}(-a_{3xu}) +$

$u_xu_{xx}u_{x\epsilon}(-3a_{3uu}) + u_xu_{xxx\epsilon}(-3a_{3u}) + u_x^2u_{xx\epsilon}(-3a_{3uu}) + u_x^3u_{x\epsilon}(-a_{3uuu}) +$

$u_xu_{xx}u_{x\delta}(-3a_{4uu}) + u_x^2u_{xx\delta}(-3a_{4uu}) + u_x^3u_{x\delta}(-a_{4uuu}) + u_{xxx}u_{x\delta}(-a_{4u}) +$

$u_{xx}u_{xx\delta}(-3a_{4u}) + u_xu_{xxx\delta}(-3a_{4u})$ \hfill (E.6)

Substituting these coefficients into (E.2) one must then impose the constraint given by the equation itself; namely solving for u_{xxxx} in (E.1) and replacing it by the right hand side everywhere it appears in (E.2). Doing this enforces the solution itself. Now, each coefficient in (E.2) (such as u_x or u_{xx}) give a system of coefficient equations for the infinitesimal generator.

With the solution to this system, one can then obtain the symmetry generator for the Lie algebra. Then integrating, one arrive at the group actions themselves. These group actions represent the symmetry transformations which take solutions for a

Appendix E. Details of Prolongation Calculation

given (x, ϵ, δ) to other solutions for different (x, ϵ', δ'). As can hopefully be seen, it is also quite straight forward to add the temporal dependence back into the calculation, though this adds another independent variable and makes the calculations even more robust.

In concluding this section, while the work on this subject is still relatively new and unfinished, the idea is promising and the general approach applicable to any non-linear wavelength selection problem. Hence, an outline is presented for future readers interested in continuing this research.

Appendix F

Photos of Experiments

F.1 Meandering System
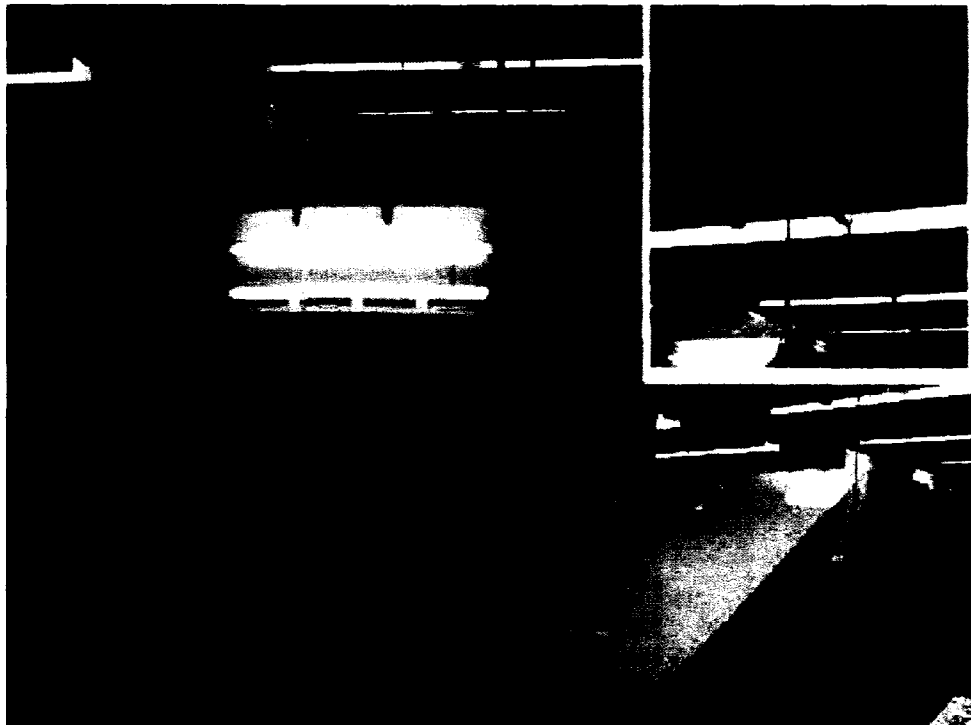
Figure F.1: The large meandering experiment set up in the Mechanical Engineering lab at the University of New Mexico
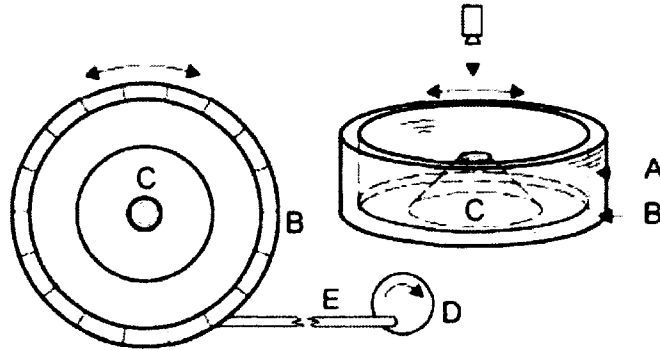
F.2   1D and 2D Sand Ripple Systems

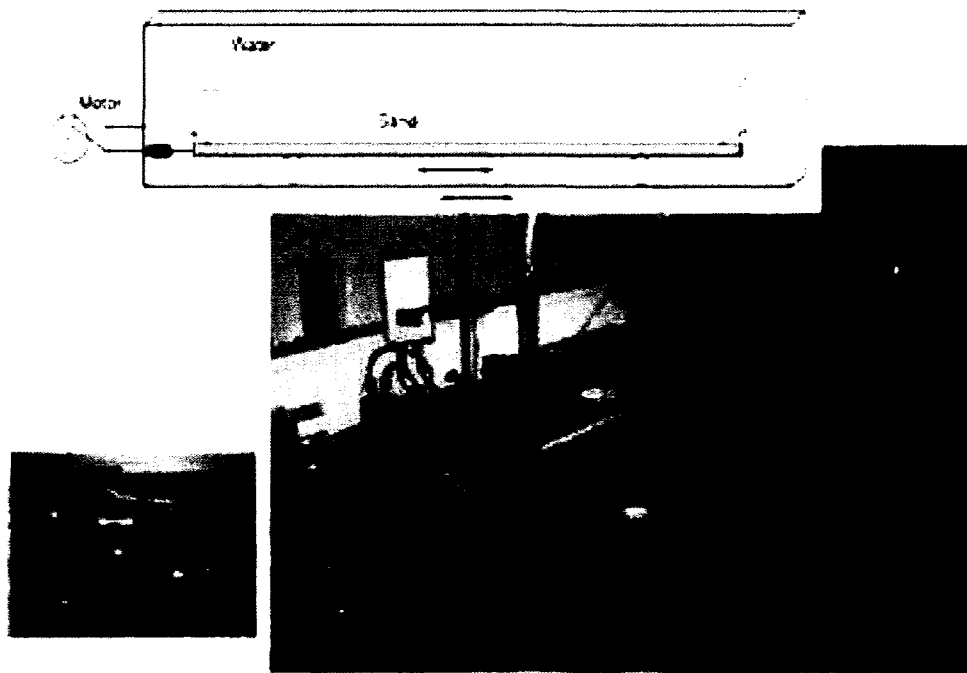Figure F.2: Schematic of circular set up.[6]

Figure F.3: Linear System [6]

While the experimental aspects and generalizations are not the work of this thesis, these results motivate the current work. Therefore, this section gives the reader a feeling for some of that work.

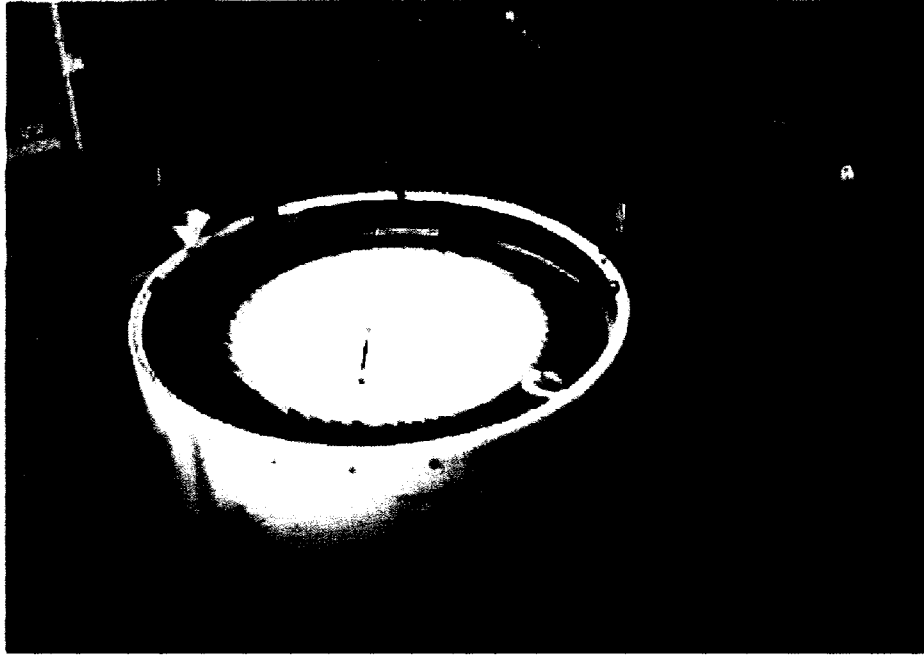In all instances the idea is similar. Drive a bed of initially flat sand with a

Figure F.4: The 2D Ripple Experiment [6]

fixed wavelength and amplitude and look at the evolution and final wavelength of the steady state solution. Also, for dynamics, studies were conducted observing transitions from one wavelength to another.

As is discussed in Section 7.6, there are several types of secondary instabilities which can occur in 2D. Experimental demonstrations of these instabilities are also presented to give the reader a picture of what this model must try to incorporate in the future.
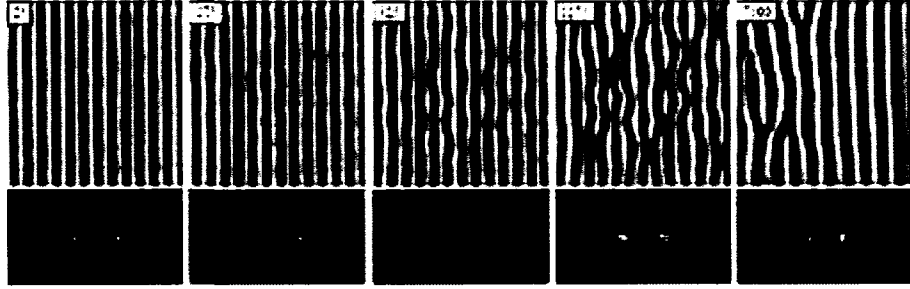
Figure F.5: The Bulging Instability: time evolution left to right, evolution of spectrum below [6]
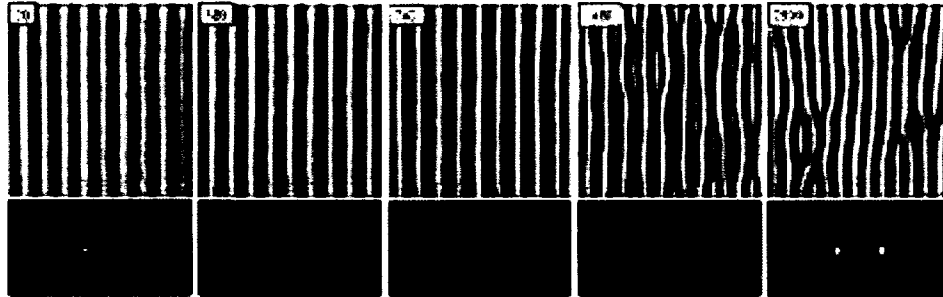

Figure F.6: Pearling Instability [6]

Figure F.7: Doubling Instability: time evolution left to right, evolution of spectrum below [6]
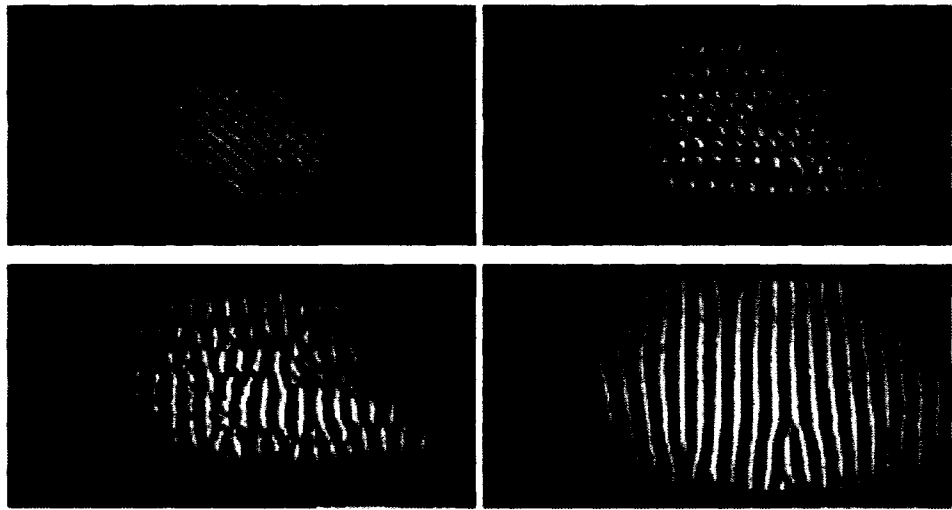
Figure F.8: Ripples driven at a skew angle to length: time evolution left to right and top to bottom [6]

Glossary

Mathematical Variables

$\mathbf{U}$: 2D fluid velocity vector (components $= (u, v)^T$)

p   : polynomial free surface profile

h   :Section 2. deviation from stream symmetry line to the center
line

Section 3. Interface profile between sand and fluid.

P : Pressure

$\hat{e}_i$: unit normal vector in direction i

$\mathbf{H}$: stochastic distribution (components η_i, $i = \{x, y\}$)

X_t : Stochastic Process (also Y_t, Z_t)

Physical Constants

l : Average stream height

w : stream width

g : gravity

ν : kinematic viscosity

ρ : fluid density

γ : coefficient of surface tension

Physical Variables

Q : volume flow rate

112

Glossary

α : inclination angle

θ : contact angle

ψ : angle between stream vector and x-axis

ϱ : angle of repose; angle of a sandpile before it avalanches

<u>Standard Conventions</u>

$< (\cdot) >$: ensemble average of $(\cdot)$

$E(\cdot)$: Expectation value of $(\cdot)$